A model-model and data-model comparison for the early Eocene hydrological cycle

M. J. Carmichael[1,2], D. J. Lunt[1], M. Huber[3], M. Heinemann[4], J. Kiehl[5], A. LeGrande[6], C. A. Loptson[1], C. D. Roberts[7], N. Sagoo[1,a], C. Shields[5], P. J. Valdes[1], A. Winguth[8], C. Winguth[8], and R. D. Pancost[2]

[1]BRIDGE, School of Geographical Sciences and Cabot Institute, University of Bristol, UK
[2]Organic Geochemistry Unit, School of Chemistry and Cabot Institute, University of Bristol, UK
[3]Climate Dynamics Prediction Laboratory, Department of Earth Sciences, The University of New Hampshire, USA
[4]Institute of Geosciences, Kiel University, Germany
[5]Climate and Global Dynamics Laboratory, UCAR/NCAR, USA
[6]NASA Goddard Institute for Space Studies, USA
[7]The Met Office, UK
[8]Climate Research Group, Department of Earth and Environmental Sciences, University of Texas Arlington, USA
[a]now at: Department of Geology and Geophysics, Yale University, USA

Received: 19 June 2015 – Accepted: 25 June 2015 – Published: 17 July 2015
Correspondence to: M. J. Carmichael (matt.carmichael@bristol.ac.uk)
Published by Copernicus Publications on behalf of the European Geosciences Union.

Abstract

A range of proxy observations have recently provided constraints on how Earth's hydrological cycle responded to early Eocene climatic changes. However, comparisons of proxy data to General Circulation Model (GCM) simulated hydrology are limited and inter-model variability remains poorly characterised. In this work, we undertake an intercomparison of GCM-derived precipitation and $P-E$ distributions within the extended EoMIP ensemble (Lunt et al., 2012), which includes previously-published early Eocene simulations performed using five GCMs differing in boundary conditions, model structure and precipitation relevant parameterisation schemes.

We show that an intensified hydrological cycle, manifested in enhanced global precipitation and evaporation rates, is simulated for all Eocene simulations relative to preindustrial. This is primarily due to elevated atmospheric paleo-CO_2, resulting in elevated temperatures, although the effects of differences in paleogeography and ice sheets are also important in some models. For a given CO_2 level, globally-averaged precipitation rates vary widely between models, largely arising from different simulated surface air temperatures. Models with a similar global sensitivity of precipitation rate to temperature (dP/dT) display different regional precipitation responses for a given temperature change. Regions that are particularly sensitive to model choice include the South Pacific, tropical Africa and the Peri-Tethys, which may represent targets for future proxy acquisition.

A comparison of early and middle Eocene leaf-fossil-derived precipitation estimates with the GCM output illustrates that GCMs generally underestimate precipitation rates at high latitudes, although a possible seasonal bias of the proxies cannot be excluded. Models which warm these regions, either via elevated CO_2 or by varying poorly constrained model parameter values, are most successful in simulating a match with geologic data. Further data from low-latitude regions and better constraints on early Eocene CO_2 are now required to discriminate between these model simulations given the large error bars on paleoprecipitation estimates. Given the clear differences between simulated precipitation distributions within the ensemble, our results suggest that paleohydrological data offer an independent means by which to evaluate model skill for warm climates.

1 Introduction

Considerable uncertainty exists in understanding how the Earth's hydrological cycle will function on a future warmer-than-present planet. State-of-the-art General Circulation Models (GCMs) show a wide inter-model spread for future precipitation and runoff responses when prescribed with the same greenhouse gas emission trajectories (IPCC, 2013; Knutti and Sedlácek, 2012). Remarkably few studies have investigated the hydrology of ancient greenhouse climates, but understanding how the hydrological cycle operated differently during these intervals could provide insight into the mechanisms which will govern future changes and the sensitivity of these processes (e.g. Pierrehumbert, 2002; Suarez et al., 2009; White et al., 2001). In particular, characterising the hydrological cycle simulated in GCMs using paleo-boundary conditions and comparisons to geological proxy data can contribute to developing an understanding of how well models that are used to make future predictions perform for warm climates.

Numerous proxy studies indicate that the early Eocene (56 – 49 Ma) was the warmest sustained interval of the Cenozoic, with evidence for substantially elevated global temperatures relative to modern in both marine (Zachos et al., 2008; Dunkley Jones et al., 2013; Inglis et al., 2015) and terrestrial settings (Huber and Caballero, 2011; Pancost et al., 2013). Beginning in the mid-Paleocene, a long-term warming trend resulted in bottom water temperatures increasing by about 6°C, culminating in the sustained warmth of the Early Eocene Climatic Optimum (EECO, 53- 50 Ma; Littler et al., 2014; Zachos et al., 2008). During the EECO, pollen and macrofossil evidence indicate near-tropical forest growth on Antarctica (Pross et al., 2012; Francis et al., 2008) and fossils of fauna including alligators, tapirs and non-marine turtles occur in the Canadian Arctic (Markwick, 1998; Eberle, 2005; Eberle and Greenwood, 2012). Absolute temperatures for the Paleogene remain controversial (e.g. Taylor et al., 2013; Douglas et al., 2014; Hollis et al., 2012), but SSTs may have reached 26–28 °C in the Southwest Pacific during this interval (TEX^{L}_{86}; Hollis et al., 2012; Bijl et al., 2009). The EECO mean annual air temperature (MAT) of Wilkes' Land margin on Antarctica has been estimated to be 16±5 °C (Nearest Living Relative, NLR, based on paratropical vegetation), with summer temperatures as high as 24–27 °C, inferred from soil bacterial tetraether lipids (MBT/CBT; Pross et al., 2012); similar but slightly higher MATs were obtained from New Zealand (Pancost et al., 2013). Low-latitude data are scarce, but oxygen isotopes of planktic foraminfera and TEX_{86} indicate SSTs off the coast of Tanzania > 30 °C (Pearson et al., 2007; Huber, 2008).Superimposed on these longer term trends were a series of briefer transient 'hyperthermal' warmings, associated with global scale perturbations to the carbon cycle. The most prominent of these was the Paleocene-Eocene Thermal Maximum (PETM; ~56 Ma) which resulted in surface warming of between 5 – 9° C above background levels (Dunkley-Jones et al., 2013; McInerney and Wing, 2011). A number of smaller amplitude hyperthermals followed, including ETM2, H2, I1, I2 and the K/X events (Cramer et al., 2003; Lourens et al., 2005; Stap et al., 2010), with the latter events occurring within the peak multi-million year warmth of the EECO (e.g. Kirtland-Turner et al., 2014). These later hyperthermals are also characterised by rapid warming and transient changes in the carbon cycle, although the environmental consequences are less well explored (e.g. Nicolo et al., 2007; Sluijs et al., 2009; Krishnan et al., 2014).

Determining the causes of warmth and simulating the climatic variability of this interval has been a major focus of paleoclimatic modelling. Whilst the role of paleogeographic changes throughout the Eocene is the subject of debate (e.g. Inglis et al., 2015; Bijl et al., 2013; Lunt et al., *In Review*), changes in greenhouse gases and carbon cycling have been widely invoked to explain both the early Eocene multi-million year warming trend and hyperthermals (e.g. Komar et al., 2013; Slotnick et al., 2012; Zachos et al., 2008). However, few proxy estimates of early Eocene atmospheric carbon dioxide exist. Paleosol geochemistry indicates concentrations could have reached ~ 3000 ppmv (i.e. > 10 x preindustrial CO_2; Yapp, 2004; Lowenstein and Demicco, 2006), whilst stomatal index approaches yield more modest values of 400–600 ppmv (i.e. 1.5 – 2 x preindustrial CO_2; Royer et al., 2001; Smith et al., 2010). Recent modelling indicates that terrestrial methane emissions also could have been significantly greater than modern, representing an additional greenhouse gas forcing (Beerling et al., 2011). Considering proxy uncertainties in both age and *p*CO2 calibration, these estimates represent a range of plausible atmospheric greenhouse gas concentrations with which to undertake GCM studies. However, simulating warm high-latitude and equable continental interior temperatures implied by temperature proxies has proven challenging, with models struggling to replicate the reduced equator-pole temperature gradient implied by the proxies (Huber and Sloan, 2001; Valdes, 2011; Pagani et al., 2013 and references therein). This has resulted in the suggestion that GCMs may be missing key heat transfer processes or mechanisms for warmth (e.g. Abbot and Tziperman, 2008; Huber et al., 2004; Korty et al., 2002; Kirk-Davidoff et al., 2002), as well as re-evaluation of existing proxy data and new modelling aimed at reducing data-model anomalies (Sagoo et al., 2013; Kiehl and Shields, 2013; Loptson et al., 2014; Sluijs et al., 2006; Huber and Caballero, 2011; Lunt et al., 2012).

Despite extensive effort to understand the causes and nature of the Eocene super-greenhouse climate state, its hydrology remains poorly characterised. Initial observations of globally widespread Eocene laterites and coals (Frakes, 1979; Sloan et al., 1992) and of enhanced sedimentation rates and elevated kaolinite in the clay fraction of many coastal sections (Bolle et al., 2000; Bolle and Adatte, 2001; John et al., 2012; Robert and Kennett, 1994; Nicolo et al., 2007) suggested early Eocene terrestrial environments were characterised by globally enhanced precipitation and runoff relative to today. Diverse geochemical proxies are now providing a more nuanced interpretation of how the spatial organisation of the Eocene hydrological cycle differed from that of the modern. This is particularly the case for the PETM. In the Arctic, the hydrogen isotopic composition of putative leaf-wax compounds became enriched by ~ 55‰ δD at the PETM, thought to reflect increased export of moisture from low latitudes (Pagani et al., 2006). Enrichment of δD in leaf waxes from tropical Tanzania, coincident with elevated concentrations of terrestrial biomarkers and sedimentation rates, has been interpreted as indicating a shift to a more arid climate with seasonally heavy rainfall (Handley et al., 2012, 2008). Whether these changes are typical of the low latitudes or are highly localised responses remains to be determined. Elsewhere, conflicting evidence for regional hydrological changes exist: an increased PETM offset in the magnitude of the Carbon Isotope Exursion (CIE) between marine and terrestrially derived carbonates, including from Wyoming, has been suggested to reflect increases in humidity/soil moisture of the order of 20–25% (Bowen et al., 2004). Other studies utilising leaf physiogonomy and paleosols suggest the North American continental interior became drier at the onset of the PETM, or alternated between wet and dry phases (Kraus et al., 2013; Smith et al., 2007; Wing et al., 2005).

These proxies collectively indicate an early Eocene hydrological cycle different to that of the modern, but only limited proxy-model comparisons have been made (Pagani et al., 2006; Speelman et al., 2010; Winguth et al., 2010). Such comparisons will be valuable for better understanding the climate of warm time intervals but also offer an alternative to temperature by which to evaluate GCM performance and/or constrain boundary conditions. Some analysis of model sensitivity of precipitation and $P-E$ to imposed CO_2 (Winguth et al., 2010), paleogeography (e.g. Roberts et al., 2009) and parametric uncertainty (Sagoo et al., 2013; Kiehl and Shields, 2013) has been undertaken, but the range of hydrological behaviour simulated within different models has not yet been assessed. Broadly, GCMs indicate that future warmth will be associated with an exacerbated P-E distribution, as increased water vapour transport occurs from moisture divergence zones into convergence zones (Held and Soden, 2006; Chou and Neelin, 2004). An intensified hydrological cycle, associated with increased meridional transport of water vapour is therefore consistent with regions of both wetting and drying, although this thermodynamic response may be complicated by dynamical shifts in atmospheric circulation (e.g. Chou et al., 2009; Bony et al., 2013; Chadwick et al., 2013). However, these hypotheses remain largely untested on ancient climate states. Lunt et al. (2012) undertook a model intercomparison of early Eocene warmth, EoMIP, based on an ensemble of 12 Eocene simulations undertaken in four fully-coupled atmosphere–ocean climate models, a summary of which is given in Table 1. This demonstrated differences in global surface air temperature of up to 9 °C for a single imposed CO_2 and differing regions of CO_2-induced warming but the implications for the hydrological cycle have not been considered.

This study addresses three main questions: (1) how do globally averaged GCM precipitation rates for the Eocene compare to preindustrial simulations and vary between models in the EoMIP ensemble? (2) How consistently do the EoMIP GCMs simulate regional precipitation and $P-E$ distributions? (3) Do differences between models affect the degree of match with existing proxy estimates for mean annual precipitation?

2 Model descriptions

The EoMIP approach of Lunt et al. (2012) is distinct from formal model intercomparison projects which utilise a common experimental design (e.g. PMIP3, Taylor et al., 2012; CMIP5, Braconnot et al., 2012). Instead, the EoMIP models differ in their boundary conditions and span a plausible early Eocene CO_2 range, utilise different paleogeographic reconstructions and specify different vegetation distributions. This is in addition to internal differences in model structure and physics, including precipitation-relevant parameterisations such as those relating to convection and cloud microstructure. Whilst this may hinder the identification of reasons for inter-model differences, the ensemble spans more fully the uncertainty in boundary conditions, which is appropriate for deep time climates such as the early Eocene.

The ensemble, summarised in Table 1, includes a range of published simulations of the early Eocene carried out with fully dynamic atmosphere–ocean GCMs. We extend the EoMIP ensemble as originally described by Lunt et al. (2012) to include simulations published by Sagoo et al. (2013), Kiehl and Shields (2013) and Loptson et al. (2014). A brief description of each model and the corresponding simulation is given below. Each model produces large-scale (stratiform) and convective precipitation separately, also summarised in Table 1. Greenhouse gases other than CO_2 are only varied in some of the simulations and are held at preindustrial levels in a number of the models; we have therefore estimated the forcing in terms of net CO_2 equivalent, detailed below.

2.1 HadCM3L

HadCM3L is a version of the GCM developed by the UK Met Office (Cox et al., 2000). Eocene simulations performed with atmospheric CO_2 at ×2, ×4 and ×6 preindustrial levels were presented by Lunt et al. (2010) in their study of the role of ocean circulation as a possible PETM trigger via methane hydrate destabilisation. In these simulations, models were integrated for more than 3400 years to allow intermediate-depth ocean temperatures to equilibrate. Both the atmosphere and ocean are discretised on a 3.75° longitude × 2.5° latitude grid, with 19 vertical levels in the atmosphere and 20 in the ocean. Vegetation is set to a fixed globally homogenous shrubland.

The effect of using an interactive vegetation model, TRIFFID (Cox, 2001), on temperature proxy-model anomalies was considered by Loptson et al. (2014) who performed simulations at ×2 and ×4 CO_2, continuations of those of Lunt et al. (2010). Within each grid cell, TRIFFID simulates the fractional coverage of five plant functional types, which in turn influences climate via feedbacks including albedo, evapotranspiration rate and carbon cycling (Cox et al., 2001). This study indicated that for a given prescribed CO_2, the inclusion of dynamic vegetation acts to warm global climate via albedo and water vapour feedbacks. We refer to these simulations as HadCM3L_T. The effect of dynamic vegetation on precipitation distributions and global precipitation rate was additionally briefly considered but comparisons to precipitation proxy data or to other models have not been undertaken.

2.2 FAMOUS

FAMOUS is an alternative version of the UK Met Office's GCM, adopting the same climate parameterisations as HadCM3L, but solved at a reduced spatial and temporal resolution in the atmosphere (Jones et al., 2005; Smith et al., 2008). Atmospheric resolution is 7.5° longitude × 5° latitude, with 11 levels in the vertical, whilst the ocean resolution matches that of HadCM3L. Both modules operate at an hourly time-step. Because of its reduced resolution, FAMOUS has been used for transient simulations with long run-times and in perturbed parameter ensembles where a large number of simulations are required (Smith and Gregory, 2012; Williams et al., 2013). Sagoo et al. (2013) used FAMOUS to study the effect of parametric uncertainty on early Eocene temperature distributions by varying 10 climatic parameters which are typically poorly constrained in climate models. Their results demonstrated that a globally warm climate with a reduced equator-to-pole temperature gradient can be achieved at 2 × preindustrial CO_2. Of the seventeen successful simulations which ran to completion, our focus is on E16 and E17, the simulations with the shallowest equator-to-pole temperature gradient and which show the optimal match to marine and terrestrial temperature proxy-data. At the ocean grid resolution, the paleogeography matches that of Lunt et al. (2010). Vegetation is set to a fixed homogenous shrubland. All simulations were run for a minimum of 8000 model years and full details of the perturbed parameters are provided in Sagoo et al. (2013). Sagoo et al. show DJF and JJA precipitation distributions for their globally warmest and coolest simulations, but comparisons to other models or to proxy data have not been made.

2.3 CCSM3

We utilise three sets of simulations performed with CCSM3, a GCM developed by the US National Centre for Atmospheric Research in collaboration with the university community (Collins et al., 2006). The first set was initially used by Liu et al. (2009) in their study of Eocene–Oligocene sea surface temperatures, and subsequently compared to terrestrial proxy data in a study of the early Eocene climate equability problem by Huber and Caballero (2011). These simulations are configured with atmospheric CO_2 at ×2, ×4, ×8 and ×16 preindustrial. Models were integrated for between 2000 and 5000 years, until the sea surface temperature was in equilibrium. The atmosphere is resolved on a 3.75° longitude by ~ $^\circ$ 3.75 latitude (T31) grid with 26 levels in the vertical and the ocean is resolved on an irregularly spaced dipole grid. The prescribed land surface cover follows the reconstructed vegetation distribution utilised in Sewall et al. (2000). Following the approach of Lunt et al. (2012) we refer to these simulations as CCSM3_H.

The second set of simulations, which we refer to as CCSM3_W, was described by Winguth et al. (2010) and Shellito et al. (2009) and conducted at ×4, ×8 and ×16 preindustrial CO_2. Relative to the CCSM3_H simulations, these simulations utilised a solar constant reduced by 0.44 %, , adopted an updated vegetation distribution (Shellito and Sloan, 2006) and utilised a marginal sea parameterisation, resulting in paleogeographic differences, particularly in polar regions. However, the major difference between the simulations is that the CCSM3_W simulations utilise a modern-day aerosol distribution, whereas CCSM3_H adopts a reduced loading for the early Eocene based on a hypothesised lower early Eocene ocean productivity (Kump and Pollard, 2008; Winguth et al., 2012).

The third set of simulations, CCSM3_K, is described in Kiehl and Shields (2013). This study investigated the sensitivity of Eocene climatology to the parameterisation of aerosol and cloud effects, specifically by altering cloud microphysical parameters including cloud drop number and effective cloud drop radii. Modern day values from pristine regions are applied homogenously across land and ocean. Simulations were performed at two greenhouse gas concentrations corresponding to possible pre- and trans-PETM atmospheric compositions which are equivalent to CO_2 of ~ ×5 and ~ ×9 preindustrial, respectively. Paleogeography and vegetation distribution are the same as those used in CCSM3_W and the solar constant is reduced by 0.487% relative to modern. Changes in precipitation distribution between high- and low-CO_2 simulations have previously been shown for the CCSM3_W and CCSM3_K simulations (Winguth et al., 2010; Kiehl and Shields, 2013), but how robust these Eocene distributions are to GCM choice remains unknown.

2.4 ECHAM5/MPI-OM

The ECHAM5/MPI-OM model is the GCM of the Max Planck Institute for Meteorology (Roeckner et al., 2003), used by Heinemann et al. (2009) in their study of reasons for early Eocene warmth. The model was configured with CO_2 at ×2 preindustrial, using the paleogeography of Bice and Marotzke (2001) and a globally homogenous vegetation cover, with lower albedo but larger leaf area and forest fraction than pre-industrial, equivalent to a modern day woody savannah. Atmosphere components are resolved on a gaussian grid with a spacing of 3.75° longitude and approximately 3.75° latitude. Relative to the preindustrial simulation, methane is increased from 65 to 80 ppb and nitrous oxide from 270 to 288 ppb for the Eocene, but these are negligible relative to change in radiative forcing associated with doubling of preindustrial CO_2. Latitudinal precipitation distributions in the simulation relative to preindustrial were considered by Heinemann et al. (2009) and elevated convective precipitation at highlatitudes suggested to be consistent with convective clouds as a high-latitude warming mechanism (Abbot and Tziperman, 2008).

2.5 GISS-ER

The E-R version of the Goddard Institute for Space Studies model (GISS-ER; Schmidt et al., 2006) was utilised by Roberts et al. (2009) in their study of the impact of Arctic paleogeography on high-latitude early Eocene sea surface temperature and salinity. Here, we include the simulation with open Arctic paleogeography of Bice and Marotzke (2001) which is also utilised in the ECHAM5 simulation. The simulation was performed with CO_2 at 4× preindustrial, and CH_4 at 7× preindustrial, equivalent of a total Eocene greenhouse gas forcing of ~ 4.3× preindustrial CO_2. The atmospheric component of GISS-ER has a grid resolution of 4° latitude by 5° longitude with 20 levels in the vertical; the ocean model is of the same horizontal resolution but with 13 levels. Vegetation is prescribed as in Sewall et al. (2000). The hydrological cycle is shown to be intensified for the Paleogene simulation, with elevated global precipitation and evaporation rates, but spatial precipitation distributions were not studied.

3 Results

3.1 Preindustrial simulations

The simulation of precipitation is a particular challenge for GCMs given the range of spatial and temporal scales at which precipitation-producing processes occur, compared to a typical model grid and timestep (e.g. Knutti and Sedlacek, 2013; Hagemann et al., 2006). Model resolution and the parameterisation schemes which account for sub-grid scale precipitation, in addition to temperature distributions, differ between the GCMs in the ensemble (Table 1). We initially summarise model skill in simulating preindustrial mean annual precipitation (MAP) to provide context for our Eocene model intercomparison and to identify which, if any, precipitation structures are unique to the Eocene, and which are more fundamentally related to errors particular to a given GCM.

Figure 1 shows preindustrial MAP distributions for each GCM in the EoMIP ensemble and anomalies for each preindustrial simulation relative to CMAP observations (Centre for Climate Prediction, Merged Analysis of Precipitation), which incorporates both satellite and gauge data (Yin et al., 2004; Gruber et al., 2000). The following observations can be made:

i. All of the EoMIP GCMs simulate the principal features of the observed preindustrial MAP distribution, although errors occur in their position and strength. The Inter-tropical Convergence Zone (ITCZ), North Atlantic and North Pacific storm tracks and subtropical precipitation minima over eastern ocean basins are identifiable for each simulation, but differences are evident between the models. Some biases are common to a number of the models, in particular those relating to the ITCZ and tropical precipitation. HadCM3L, FAMOUS, ECHAM5 and CCSM3 all simulate the ITCZ mean annual location north of the Equator, but the South Pacific Convergence Zone (SPCZ) generally extends too far east in the Pacific, and is too zonal, with precipitation equalling that to the north of the Equator to produce a "double-ITCZ" – a common bias in GCMs (Dai, 2006; Lin et al., 2007; Brown et al., 2011). The localised rain belt minimum is a result of the Pacific cold-tongue, not present in GISS-ER, which instead simulates a single convergence zone with high mean annual precipitation across the tropics. Other biases which appear common across the ensemble include too little precipitation over the Amazon (Yin et al., 2013; Joetzer et al. 2013), over-precipitation in the Southern Ocean (Randall et al., 2007 and references therein) and biases in the position of rainfall maxima in the Indo-Pacific (e.g. Liu et al., 2014).

ii. Errors over the continents are less than those over the oceans. Absolute errors in MAP are largest over the high precipitation tropical and subtropical oceans, and frequently exceed 150 cm year^{-1} in the case of ITCZ and SPCZ offsets. Over the continents, anomalies are generally no greater than 60 cm year^{-1} and more than 80% of the multimodel mean terrestrial surface has an anomaly less than 30 cm year^{-1}. In low precipitation regions, these errors still result in significant percentage errors (Fig. S1).

iii. Models show regional differences in precipitation skill. Figure 1 demonstrates that some precipitation biases are individual to particular GCMs. Whilst these are most noticeable over the high precipitation tropical and subtropical oceans, such as offsets in the location of maximum precipitation intensity or strength of storm tracks, relative differences within low-precipitation continental regions can also be considerable (Mehran et al., 2014; Phillips and Gleckler, 2006). This is particularly the case for the Sahel region of northern Africa and the Antarctic continental interior (Fig. S2). We hypothesise that GCMs applied to the study of paleoclimates are also likely to show significant regional differences in their precipitation distribution, underlining the importance of model intercomparison. Given that all of the models simulate the principal features of MAP distribution, we carry all forward to our Eocene analysis. However, it is important to recognise that significant model biases in simulating precipitation distribution exist, even where boundary conditions are well constrained.

3.2 Sensitivity of the global Eocene hydrological cycle to greenhouse gas forcing

The EoMIP model simulations were configured with a range of plausible early Eocene and PETM atmospheric CO_2 levels, yielding a range of global mean surface air temperatures (Lunt et al., 2012). It is therefore possible to evaluate how consistently precipitation rates are simulated across the GCMs (i) for a given CO_2, (ii) for a given global mean temperature, or in the case of those models for which multiple simulations have been performed, (iii) for a given CO_2 change and (iv) for a given global mean temperature change. Closure of the GCM global hydrological budget requires that total annual precipitation and evaporation are equal, providing there is no net change in water storage – the imbalances, summarised in Table S1 are < 0.01 mm day^{-1} equivalent. . Mean annual global precipitation rate therefore provides a zero-order indication of the intensity of the global hydrological cycle. Precipitation rates calculated from three modern observational datasets are shown in Fig. 2b (open circles); model-estimated rates derived from preindustrial simulations (filled circles) are in relatively good agreement with observational data, providing confidence in this measure.

All of the EoMIP models exhibit a more active hydrological cycle for the Eocene (Fig. 2b; squares) compared to that simulated in the corresponding preindustrial simulations (Fig. 2b; circles). For a given CO_2, the models vary in the intensity of the hydrological cycle they simulate; for example, ECHAM5 has a global precipitation rate at 2 × preindustrial CO_2 comparable to that of CCSM3_W at ~ 12×preindustrial CO_2. In the remainder of this section, we discuss reasons for these differences, which can be attributed to (i) differences in Eocene boundary conditions, including CO_2 (ii) variation of poorly constrained parameter values and (iii) more fundamental differences in the ways in which the models simulate hydrology.

The GCMs within the EoMIP ensemble differ in their global mean temperature for a given CO_2 (e.g. Lunt et al., 2012; Fig. 2a). Consequently, the global precipitation rate for each ensemble member is shown in Fig. 2c relative to its globally averaged surface air temperature. This demonstrates that much of the variation between models in precipitation rate arises from these temperature differences. For example, the elevated precipitation rate in the 2×CO_2 ECHAM5 is explained by this model's warmth, being globally > 5 °C warmer than HadCM3L at the same CO_2.

Similarly, the enhanced precipitation rate in the CCSM3_K simulations at both ~ ×5 CO_2 and ~ ×9 CO_2 relative to those simulated in CCSM3_H and CCSM3_W are attributable to warmer surface temperatures in CCSM3_K, resulting from alterations to cloud condensation nuclei (CNN) parameters, with a reduction in low-level cloud acting to increase short-wave heating at the surface (Kiehl and Shields, 2013). The reduced aerosol loading in CCSM3_H results in surface warming relative to CCSM3_W (Fig. 2a), which explains much of the 7–8% increase in strength of the hydrological cycle across the CO_2 range studied. There are effects beyond those induced by surface temperature, however. For example, for a given surface air temperature, the global precipitation rate is consistently weaker in CCSM_W relative to CCSM_H (Fig. 2c) – possibly a result of modified aerosol-cloud interactions due to the changes in prescribed aerosols in CCSM_H.

The degree to which the global hydrological cycle will intensify with future global warming has received much attention (e.g. Allen and Ingram, 2002; Held and Soden, 2006; Trenberth, 2011). Held and Soden (2006) show a ~ 2% increase in global precipitation per degree of warming for AR4 GCMs forced with the A1B emissions scenario, but with notable inter-model variability. For those simulations with multiple CO_2 forcing, it is possible to estimate how this sensitivity varies for the Eocene. We show the d*P/*d*T* relationships for each model as well as the increase in % precipitation for a 1 °C temperature increase over the range of 15–30 °C (Table 2). Both CCSM3 and HadCM3L appear to be broadly comparable at ~ 1.8–2.1% increase in the intensity of the hydrological cycle for each degree of warming, consistent with the future climate simulations.

Some variation in the intensity of the hydrological cycle simulated by the EoMIP models may be expected to occur independently of global mean surface air temperature. For preindustrial conditions, boundary conditions are largely constant across the simulations (atmospheric composition, continental positions, orography and ice sheet distribution), yet the simulations show a spread of ~ 0.30 mm day^{-1} – which exceeds the precipitation increase for a doubling of CO_2 from ×2 to ×4 preindustrial in both CCSM3_H (0.13 mm day^{-1}) and HadCM3L (0.18 mm day^{-1}). Differences in global precipitation rate between the preindustrial simulations are not explained by differences in temperature (Fig. 2b) but may relate to more fundamental differences in model physics, particularly between HadCM3L and CCSM3W given that a more active hydrological cycle is consistently simulated in HadCM3L for both the Eocene and preindustrial conditions. Further simulations using equivalent precipitation parameterisation schemes for large-scale and convective precipitation would be required to fully evaluate this hypothesis.

For both the ×2 and ×4 CO_2 simulations, the HadCM3L simulations that include the TRIFFID dynamic vegetation model have a near identical precipitation rate to those without (Fig. 2b). However, the ×4 CO_2 simulation with dynamic vegetation is substantially warmer than the ×4 simulation with fixed homogenous shrubland. The inclusion of the dynamic vegetation model acts to warm the surface climate as described in Loptson et al. (2014), but this does not yield an associated increase in precipitation. Relative to the fixed shrubland simulations, the TRIFFID simulations show a reduction in continental evapotranspiration in response to doubling of CO_2, which results in diminished moisture availability over the tropical landmass, for a given temperature (Fig S3). The TRIFFID simulations therefore exhibit a reduced hydrological sensitivity of only ~ 1.3% increase in precipitation per degree of warming (d*P/*d*T*) compared with ~ 1.8% for the non-TRIFFID simulations.

In the FAMOUS simulations undertaken by Sagoo et al. (2013; Fig. 2d), all simulations are performed at 2×CO_2, but global temperatures range between 12.3 and 31.8 °C on account of simultaneous variation of 10 uncertain parameter values, some of which directly influence cloud formation and precipitation. Within these simulations there is also a linear relationship between surface air temperature and global precipitation (R^2 = 0.965; *n* = 17) suggesting the global intensity of the hydrological cycle remains primarily coupled to global temperature, despite greater scatter around the d*P/*d*T* relationship. Despite this, the overall d*P/*d*T* relationship in FAMOUS is higher than that of HadCM3L and HadCM3L+TRIFFID, with a ~ 2.8% increase in precipitation for each degree of warming (Table 2).

In HadCM3L, the 1×CO_2 Eocene and preindustrial simulations have similar global precipitation rates (Fig. 2a), implying that Eocene boundary conditions other than CO_2 do not exert a major influence on the intensity of the hydrological cycle, raising global precipitation rate by only ~ 0.10 mm day^{-1}. Moreover, even this small increase is consistent with and likely driven by a small increase in global surface air temperature. Furthermore, the preindustrial simulations for both CCSM3 and HadCM3L lie on, or close to, the Eocene-derived d*P/*d*T* lines (Fig. 2c), suggesting that globally, precipitation rate for a given temperature is not increased/decreased for the Eocene, despite differences in low-latitude land–sea distribution, ocean gateways and a lack of Eocene ice sheets. Intriguingly, extrapolating the d*P/*dCO_2 relationship backwards to 1×CO_2 for CCSM_W would require an Eocene precipitation rate ~ 7% above that of the preindustrial rate. This suggests a more substantial effect of Eocene boundary conditions on elevating absolute precipitation rates for CCSM3_W than that seen in HadCM3L, but still operating via temperature effects. GISS-ER has a marginally more vigorous hydrological cycle than the other models for a given global temperature. Roberts et al. (2009) show that the global precipitation rate in a preindustrial 4×CO_2 simulation in GISS-ER is ~ 4% greater than that of the preindustrial, whereas the Paleogene simulation has a precipitation rate ~ 23% above that of the preindustrial. Therefore non-greenhouse gas Paleogene boundary conditions are crucial in elevating precipitation rate in this model, in contrast to HadCM3L. However, this also appears to be mediated by temperature effects, given that the Eocene simulations of Roberts et al. (2009) are also substantially warmer than preindustrial geography simulations with 4 x CO_2 greenhouse gas concentrations.

3.3 Variability in mean annual precipitation (MAP) distribution

3.3.1 Spatial distribution of MAP

Figure 3 shows MAP distributions for each EoMIP simulation. Eocene distributions are relatively similar to those for preindustrial conditions (Fig. 1), with clearly recognisable inter-tropical convergence zone (ITCZ)and South Pacific convergence zone (SPCZ) structures, and subtropical precipitation minima, the distributions of which appear to be longstanding characteristics of Cenozoic precipitation. Relative to preindustrial simulations, the Eocene distributions exhibit increased precipitation at high latitudes as a consequence of elevated temperatures in these regions. In CCSM in particular, the Eocene is characterised by a more globally equable precipitation rate: the expansion of zones of highest precipitation in the Eocene relative to preindustrial is muted compared with a more extensive loss of low precipitation regions. Additional support for this is provided by a comparison of mean precipitation rates for land and ocean (Table S2). The preindustrial ratio of land : ocean precipitation is maintained in the Eocene HadCM3L and ECHAM simulations, whereas in CCSM, precipitation rates over land and ocean are typically equal. The effects of differences in simulated surface air temperatures between models within the ensemble are also evident: for a given global surface temperature, HadCM3L maintains cooler poles than CCSM3 and ECHAM5 (Sect. 3.3.2) and regions with MAP< 300 cm year^{-1} persist in the Arctic and Antarctic, even at ×4 CO_2.

Modelled Eocene MAP features are frequently traceable to those identified in preindustrial simulations (Sect. 3.1), including the single tropical convergence zone in the GISS ×4 CO_2 simulation and the double ITCZ in a number of the models. Elsewhere, the Eocene precipitation distributions diverge from those of the preindustrial simulations and may be related to specific Eocene paleogeography, elevated CO_2, or other boundary conditions. In HadCM3L, there is a clear trend towards a more south-easterly trending SPCZ in the higher CO_2 simulations, which is not replicated in the warm simulations of the sister model FAMOUS. The SPCZ in CCSM is also far weaker in the Eocene simulations, compared to preindustrial simulations. The mechanisms which control the SPCZ in the modern day, particularly its northwest-southeast orientation, are only partially understood with zonal SST gradients, intensity of trade winds and the height of the Andes all suggested to be important influences (Matthews et al., 2012; Cai et al., 2012). In the EoMIP simulations, CCSM3 shows much slacker surface winds at the equator with reduced low-level convergence, whilst HadCM3L maintains stronger convergence of south-easterly trade winds with north-easterlies originating from the Pacific subtropical high (Fig S4). Despite similar preindustrial precipitation distributions over tropical Africa, CCSM and HadCM3L strongly diverge in the Eocene, with CCSM showing far more intense equatorial precipitation. In CCSM, evaporation is consistently less than the precipitation rate, which likely results in recharge of soil moisture throughout the year and an availability of moisture for convective precipitation. The FAMOUS simulations E16 and E17 represent two realisations of very warm climates with a reduced equator-pole temperature gradient – in these simulations significant increases in mid-latitude precipitation are particularly accentuated over the Pacific Ocean; increases in convection in the subtropics and mid-latitudes are sufficient to eliminate the precipitation minima seen in other models at these latitudes.

For a given CO_2, differing boundary conditions, parameterisation schemes and simulated model air temperatures prevent direct assessment of whether Eocene regional precipitation distributions are robust to GCM choice. Model simulations have a substantially different amount of water vapour in the atmosphere and differing global precipitation rates and it is not meaningful to average these simulations. Instead, we show a multimodel mean in Fig. 5 for simulations with a common global precipitation rate to provide an assessment of regional variability between model simulations with the same global strength hydrological cycle. Elevated high-latitude precipitation for the early Eocene relative to preindustrial conditions is robust between GCMs, although absolute values remain variable between models, particularly in the Southern Hemisphere, likely due to differing Antarctic orography. Differences between models in the midlatitudes are smaller, resulting in some confidence that the secondary precipitation maxima were polewards of their preindustrial location during the Eocene. Equatorial precipitation remains highly variable between models but is accentuated relative to preindustrial.

3.3.2 Controls on precipitation distribution

Precipitation rates for each simulation are summarised in Table S2, including separate rates calculated over land and ocean surfaces and rates deconvolved into those arising from convective and large-scale contributions. These data show that elevated precipitation rates in the high CO_2 Eocene simulations are largely the result of increased convection, although in the ECHAM5 model a greater percentage of precipitation is generated by large scale mechanisms in both the Eocene and preindustrial simulation. Figure 4 shows how convective and large-scale precipitation rates vary with latitude for a selection of the EoMIP simulations. This reveals differences between models in the mechanisms responsible for precipitation distributions which can be related to surface air temperature distributions. In the HadCM3L simulations, the mid-latitude maxima in both large scale and convective precipitation advance polewards with increasing CO_2 with precipitation increases over the high northern latitudes driven almost exclusively by enhanced large-scale precipitation. CCSM3 has substantially warmer poles which results in much enhanced high-latitude large scale precipitation relative to HadCM3L, although large scale latitudinal contributions differ somewhat for preindustrial simulations at both low and high latitudes. In CCSM3_K, the warmest CCSM3 simulations, polar temperatures are elevated compared to CCSM3_H as is total precipitation in these regions, but in this case large scale precipitation is reduced over much of the high latitudes and the higher total precipitation is due to convective processes. Mid-latitude precipitation maxima within the ECHAM5 simulation arise from large-scale mechanisms rather than convection; however, this is also true of the preindustrial simulation and does not relate to Eocene boundary conditions.

In the warmest FAMOUS simulations of Sagoo et al. (2013), the high latitudes experience particularly significant increases in large scale precipitation, such that the maximum values are those at the poles in the E17 simulation, and in the Southern Hemisphere the local mid-latitude precipitation maximum is lost. Elevated mid-latitude temperatures in the warm FAMOUS simulations additionally result in significant increases in convective precipitation which are not simulated in the cooler simulations and models. Overall, convective precipitation in FAMOUS increases as both global temperatures rise and equatorial-to-polar temperature gradients decrease, regardless of the underlying parameter configuration; this emphasises the fundamental control of temperature distribution on precipitation, as opposed to the effect of alteration of any one specific parameter.

Improvements in the simulation of precipitation in modern day climate simulations are often related to better resolved topography (e.g. Gent et al., 2010). However, given the variety of differences in boundary conditions between the EoMIP simulations, topography appears to only have limited power in explaining differences between regional precipitation responses. Figure S5 shows differences in topography and precipitation rate between three sets of simulations with similar global precipitation rates: (i) HadCM3L and FAMOUS – where the models have similar parameterisation schemes but differ in atmospheric grid resolution; (ii) CCSM3_W and HadCM3L – different models, but with a similar resolution; (iii) CCSM3_W and CCSM3_H – the same model but slightly different topographic boundary conditions. The HadCM3L and CCSM3_W simulations show some substantial differences in the topography around the Rockies, with the increased elevation in CCSM3 possibly accounting for the increased precipitation in this region. However, differences in topography over the Asian subcontinent do not result in any systematic differences in precipitation rate. Regions of similar topography elsewhere, including over the Tropics, have far more divergent precipitation responses between the models, which do not relate to local differences in topography.

For HadCM3L and CCSM3, simulations at different CO_2 concentrations provide an insight into how regional Eocene precipitation distributions are impacted by warming, and anomaly plots for high – low CO_2 simulations are shown in Fig. 6. For the same CO_2 forcing, CCSM3 is globally cooler than HadCM3L (Lunt et al., 2012), but the anomalies for 16 – 4 CO_2 (CCSM_W) and 6 – 2 CO_2 (HadCM3L) display similar global changes in both temperature and therefore precitation rate on account of similar dP/dT relationships (Fig. 2; Table 2). Intriguingly, HadCM3L displays far greater spatial contrasts in net precipitation change, particularly over the ocean: between the pair of HadCM3L simulations, some 23% of the Earth's surface experiences an increase or decrease in precipitation greater than 60 cm year^{-1}, compared to just 6% in the CCSM3 simulations. Ignoring differences in the spatial pattern of atmospheric circulation - such as those relating to differing SPCZ (Sect 3.3.1), the underlying response appears to be an increase in precipitation in the deep tropics and a reduction in precipitation in the subtropics, at least over the Pacific Ocean. This increase in moisture in the convergence zone and decrease in the divergence zones appears to relate to a more vigorous change in tropical atmospheric circulation in the HadCM3L model relative to CCSM3 (Fig S6) Spatial patterns are additionally model dependent: in HadCM3L, there is a clear increase in the strength of storm tracks along the eastern Asian coastline, which is not repeated in CCSM. In HadCM3L, decreases in precipitation occur around the Peri-Tethys and along the coastline of equatorial Africa. Therefore, although models within the EoMIP ensemble exhibit similarities in their global rate of precipitation change with respect to temperature, regional precipitation distributions are strongly model dependent

3.4 Precipitation seasonality

The evolution and timing of the onset of global monsoon systems in the Eocene has been the subject of debate (Licht et al., 2014; Sun and Wang, 2005; Wang et al., 2013). Proxy studies for the early Eocene have highlighted differences in precipitation seasonality relative to modern conditions (Greenwood et al., 2010; Greenwood, 1996; Schubert et al., 2012) and geochemical and sedimentological changes at the PETM has also been attributed to changes to seasonality (Sluijs et al., 2011; Schmitz and Pujalte, 2007; Handley et al., 2012). Previous modelling work utilising CCSM3 has suggested that much of the mid-late Eocene was monsoonal, with up to 70% of annual rainfall occurring during one extended season in North and South Africa, North and South America, Australia and Indo-Asia (Huber and Goldner, 2012). However, GCMs have been shown to differ greatly in their prediction of future monsoon systems (e.g. Turner and Slingo, 2009; Chen and Bordoni, 2014), and therefore we examine the similarities and differences in Eocene models with respect to the seasonality of their precipitation distributions.

Figure 7 shows the percentage of precipitation falling in the extended summer season (MJJAS for Northern Hemisphere; NDJFM for Southern Hemisphere) following the approach of Zhang and Wang (2008) and also utilised in the Eocene studies of Huber and Goldner (2012) and Licht et al. (2014). This metric has been shown to correlate well with the modern-day distribution of monsoon systems. Overall, the models show a global distribution of early Eocene monsoons in high CO_2 climates that is similar to those simulated under preindustrial simulations (Fig. S7). Australia is markedly less monsoonal than in preindustrial simulations due to its more southerly Eocene paleolocation. Note that regions where winter season precipitation dominates fall at the lower end of the scale; these tend to be over the ocean surface but also include regions around the Peri-Tethys and both the Pacific and Atlantic US coasts.

HadCM3L is notable in that it is more seasonal at high latitudes, simulating an early Eocene monsoon centred over modern day Wilkes' Land region of Antarctica. Although proxy data have suggested highly seasonal precipitation regimes for both the Arctic (Schubert et al., 2012) and Antarctic (Jacques et al., 2014) during this interval, these systems are maximised in the ×2 CO_2 simulation and weaken somewhat in the simulations with elevated CO_2. This arises due to the high temperature seasonality of Arctic/ Antarctic Eocene regions in HadCM3L relative to the other models (e.g., Gasson et al., 2013). In austral winter, Antarctic temperatures are sufficiently low to suppress precipitation, whilst this constraint is lifted somewhat in the higher CO_2 simulations which produce more equable rainfall distribution. Crucially, the effect of elevated global warmth on the extent of Eocene monsoons is consistent across the models, with higher CO_2 simulations associated with a decline in terrestrial areas with seasonal precipitation regimes (Table 3). HadCM3L simulates a 6% reduction in the extent of terrestrial regions influenced by monsoonal regimes for the Eocene (HadCM3L ×1 CO_2) relative to the preindustrial simulation; this reduction appears to be related to the warmer surface temperatures and absence of Antarctic ice sheet.

3.5 $P-E$ distributions

The difference between precipitation and evaporation ($P-E$) is essential for understanding the wider impacts of an enhanced Eocene hydrological cycle. Over land, this parameter broadly determines how much of precipitation will become soil water and surface runoff, the partitioning itself being dependent on the land surface and vegetation schemes within the models (e.g. Cox et al., 1998; Oleson et al., 2004). Over the ocean, $P-E$ drives differences in salinity which can affect the Eocene ocean circulation (Bice and Marotzke, 2001; Waddell and Moore, 2008). We show mean annual ($P-E$) budgets for each of the EoMIP simulations in Fig. 8. In warmer climates, an exacerbation of existing ($P-E$) is expected – that is, the wet become wetter and the dry drier, as the moisture fluxes associated with existing atmospheric circulations intensify (Held and Soden, 2006). Broadly, the EoMIP simulations support this paradigm for the Eocene relative to preindustrial (Fig. 5). CCSM3 shows fairly minor changes in the boundaries between net-precipitation and net-evaporation zones at higher CO_2 (Fig. 8), although the net-evaporation zones in HadCM3L do migrate polewards over the eastern Pacific and North Atlantic at high CO_2. Other dynamic changes within HadCM3L are coupled to the precipitation responses: the more meridionally-orientated SPCZ results in a weaker zonally averaged Southern Hemisphere evaporative zone and the expansion of precipitation along the Asian coastline results in a more positive ($P - E$) balance in this region. Over continents the models also display different responses of *P-E* to warming. For example, over equatorial and northern Africa, HadCM3L simulates increasingly wet climates in the high CO_2 simlations, driven by increases in precipitation coupled to reductions in evaporation. In CCSM3, the net moisture balance is less responsive with respect to temperature, although intense equatorial precipitation means this region is much wetter than in HadCM3L.

Because of the large latent heat fluxes involved in evaporation and condensation, the global hydrological cycle acts as a meridional transport of energy. Net evaporation in the subtropics stores energy in the atmosphere as latent heat, releasing it at high latitudes via precipitation (Pierrehumbert, 2002). An intensified hydrological cycle, associated with increased atmospheric transport of water vapour, has therefore been suggested as a potential mechanism for reducing the equator-pole temperature gradient during greenhouse climates (Ulfnar et al., 2004; Caballero and Langen, 2005). By integrating the area-weighted estimates of $P - E$ with latitude, we show how these contributions differ between the EoMIP models and associated preindustrial simulations (Fig. 9). Relative to preindustrial climatology, the intensification of the hydrological cycle associated with increased drying in the net-evaporative zones and increased moistening of the net-precipitation zones implies a stronger latent heat flux. Within the EoMIP ensemble, the implied high polewards energy fluxes of the E16 and E17 FAMOUS simulations and ×2 CO_2 ECHAM simulation are particularly significant. GISS-ER has a particularly strong low-latitude equatorially-directed latent heat transfer which arises from the much elevated Eocene precipitation rate in the deep tropics. The asymmetry in some of the models' implied flux is due to a hemispheric imbalance in precipitation/evaporation. For example, in FAMOUS e17 simulation, there is greater precipitation than evaporation in the southern hemisphere and so more energy is released from the atmosphere by latent heat than is stored, meaning that the implied heat flux does not cross zero at the equator. However, since total precipitation is equal to total evaporation globally (Table S1), this is balanced out in the northern hemisphere; note that the intense evaporation zone over the North Atlantic is not matched in the Southern Hemisphere for this model. In the majority of the other models, there is greater symmetry in P-E with latitude and the implied flux crosses close to the origin of the graph on Figure 9.

At face value, it may seem that the elevated latent heat transport at mid to high latitudes could contribute towards the reduced equator-pole temperature gradient in the EoMIP simulations, but we note that theoretical and modelling based studies suggest increased latent heat transport is associated with an increased equator-pole temperature gradient (Pagani et al., 2014). Within the EoMIP ensemble, meridional temperature gradients and global surface air temperatures covary and so it is not possible to separate clearly the effects of these different controls (Fig. S8). Nevertheless, these results illustrate that relative to preindustrial, the Eocene hydrological cycle acts to elevate the meridional transport of latent heat, particularly around 45–50° N/S of the equator.

4 Proxy-model comparison

A range of proxy data provide constraints on how the early Eocene hydrological cycle differed to that of the modern, including oxygen isotopes from mammalian, fish and foraminiferal fossils (Clementz and Sewall, 2011; Zachos et al., 2006; Zacke et al., 2009) and the distribution of climatically sensitive sediments (e.g. Huber and Goldner, 2012). Changes in regional hydrology at the PETM have also been inferred from geomorphological (John et al., 2008; Schmitz and Pujalte, 2007), biomarker (Handley et al., 2011; Pagani et al., 2006) and microfossil (Sluijs et al., 2011; Kender et al., 2012) proxies. These have resulted in qualitative interpretations of hydrological change, although the climatic variables and temporal signal the proxies record are often uncertain (e.g. Handley et al., 2011, 2012; Tipple et al., 2013; Sluijs et al., 2007). However, quantitative estimates of mean annual precipitation (MAP), derived from micro- and macro-floral fossils have been made for a number of early Eocene and PETM-aged sections which can be compared directly with the GCM-estimated precipitation rates described in Sect. 3.

Paleoprecipitation estimates are primarily produced by two distinct paleobotanic methods – leaf physiogonomy and nearest living relative (NLR) approaches. In the former, empirical univariate and multivariate relationships have been established between the size and shape of modern angiosperm leaves and the climate in which they grow, with smaller leaves predominating in low precipitation climates (e.g. Wolfe, 1993; Wilf et al., 1998; Royer et al., 2005). The NLR approach estimates paleoclimate by assuming fossilised specimens have the same climatic tolerances as their presumed extant relatives. This approach can utilise pollen, seeds and fruit in addition to leaf fossils (Mosbrugger et al., 2005). Relative to mean annual air temperature, geologic estimates of MAP are less precise, which may relate to decoupling between MAP and local water availability (Peppe et al., 2011; Royer et al., 2002), a greater importance of growing season climate (Mosbrugger and Utescher, 1997) or in the case of physiogonomical approaches, competing influence of other climatic variables on leaf form(Royer et al., 2007).

Our data compilation is provided in Table S3. Some of the data has been compared previously with precipitation rates from an atmosphere-only simulation performed with isoCAM3 for the Azolla interval (~ 49 Ma; Speelman et al., 2010). Our proxy-model comparison includes data for the remainder of the early-mid Eocene, including a number of recently-published estimates such that the geographic spread is widened to include estimates from Antarctica (Pross et al., 2012), Australia (Contreras et al., 2013; Greenwood et al., 2003), New Zealand (Pancost et al., 2013), South America (Wilf et al., 2005) and Europe (Eldrett et al., 2014; Mosbrugger et al., 2005; Geisental et al., 2011). We select Ypresian-aged data where multiple Eocene precipitation rates exist, including estimates for the PETM (Pancost et al., 2013), but additionally include some Lutetian and Paleocene data, particularly in regions where Ypresian data does not exist. This approach is justified in some respects given the range of plausible Eocene CO_2 with which simulations have been performed. However, each data point is an independent estimate of precipitation for a given point in time and direct comparisons between data points are hindered given that considerable climatic change occurred throughout this interval (e.g. Zachos et al., 2008; Littler et al., 2014); comparisons are particularly difficult at sites where age control is poor and the proxies could potentially reflect a range of climatic states or atmospheric CO_2 (Sect 1).

Figure 10 shows paleobotanical estimates for MAP for a range of the data in Table S3, along with model-estimated rates for each of the EoMIP simulations. Mean precipitation estimates from each model are derived by averaging over grid boxes centred on the paleolocation in a similar approach to Speelman et al. (2010). This is a nine cell grid of 3×3 gridboxes for HadCM3L, GISS, ECHAM and CCSM3, although in some instances an eight cell grid of 2×4 is used along paleocoastlines. Differing model resolutions and land–sea masks result in averaging signals from slightly different paleogeographic areas, but this approach allows for an assessment of the regional signal and error bars are included to show the range of precipitation rates present within the locally defined grid. In the reduced resolution model, FAMOUS, mean and range are derived from 2×2 gridboxes to ensure regional climatologies remains comparable. Error bars on the geologic data are generally provided as described in the original publications, with further details also provided in Table S3.

Our results confirm different regional sensitivities across the models. For example, over New Zealand (Fig. 10b), HadCM3L shows a strong sensitivity to increases in CO_2, whereas in CCSM3, elevated CO_2 has little effect on precipitation rate. This arises from differing SPCZ precipitation structures, with HadCM3L simulating a shift of the rain-belt towards New Zealand in the warmer simulations (Fig. 6). Conversely, in the Western US (Fig. 10g), HadCM3L precipitation is stable with respect to increases in CO_2 whilst CCSM3 produces increases in precipitation in higher CO_2 simulations. Furthermore, significant variations occur between the degree of match the models show with proxy precipitation estimates. At grid boxes corresponding to modern day Axel Heiberg Island (Fig. 10h), HadCM3L and GISS-ER are unable to produce sufficient precipitation, whereas the high CO_2 CCSM3 and E16/17 FAMOUS simulations are in closer agreement. Over Wilkes Land, Antarctica, all of the EoMIP models show sensitivity to CO_2, but all produce too little precipitation, although the FAMOUS and CCSM_K simulations with warmer polar temperatures (Fig. 4) come closest to replicating the central estimates of geologic data. However, some caution is required in how these differences are interpreted, given that preindustrial GCM errors are also typically of the order of 300 mm year^{-1} too little precipitation over this region. A similar pattern is apparent in the Paleocene North West Territory data (Fig. 10l), with the models using low CO_2 and/or yielding cooler polar temperatures showing a dry bias. At the mid-latitudes, model biases relative to paleoprecipitation estimates are reduced, including for the continental US (Fig. 10f), Argentina (Fig. 10g) and central Europe (Fig. 10m), where proxy data are within the precipitation range simulated across the suite of simulations.

At Tanzania (Fig. 10e), all model simulations appear to overestimate precipitation and in a number of models elevating CO_2 has relatively little impact on precipitation rate. In the HadCM3L simulations in particular, elevating CO_2 to levels required to produce a match with early Eocene high-latitude data results in considerable over-precipitation at this low-latitude site, although it should be noted that the Mahenge data are likely mid-Eocene in age, and could be representative of a lower CO_2 climate. With a scarcity of low-latitude data, this interpretation remains tentative, particularly given that a number of the models show a marginal preindustrial wet bias over tropical Africa (Fig. 1) and leaf physiognomic methods tend to result in lower precipitation estimates than those provided by other proxies (e.g., Peppe et al., 2011).

The most robust observation from our comparison is that the models produce too little precipitation at locations corresponding to Eocene high-latitude sites This is consistent with suggestions that GCMs fail to simulate high-latitude warmth for the Early Eocene. If high-latitude temperatures are too cold in the model, then the saturation vapour pressure of the atmosphere is suppressed. We demonstrate this coupling of data-model temperature and precipitation errors in Fig. 11. In HadCM3L, increasing CO_2 from ×2 to ×6 decreases temperature and precipitation proxy-model differences at the majority of sites, resulting in better overall match to the geologic data. In the case of CCSM3, a relatively good match with precipitation proxy estimates is achieved at both low and high CO_2, but models appear too cold at low CO_2. In FAMOUS and CCSM3_K, parameter sets which reduce the equator-pole temperature gradient and warm the high latitudes are able to minimise errors in both temperature and precipitation with the majority of the geologic data at low CO_2. However, in FAMOUS, E17 simulates surface air temperatures> 45 °C in Colombia, which produces a significant temperature data-model anomaly. Whilst our compilation allows for some degree of model intercomparison, it is far from a global data set, with a bias towards mid and high latitude sites, and a lack of data from low latitudes (Fig. 12; Fig S9). Caution is also required in interpretation given that the data points span the early to mid-Eocene. Although few are dated to the hyperthermals (Table S3), considerable climatic change occurred throughout this dynamic interval (Section 1) and the data cannot be assumed to reflect a single CO_2 forcing. There is therefore a need for further proxy-model comparisons to corroborate our analysis.

An alternative explanation for the data-model mismatch is that the proxies from high latitudes are seasonally biased recorders of precipitation. The seasonality of the Canadian Arctic during the early Paleogene has been the subject of much interest, with indicators such as reptile and *Coryphodon* fossils suggesting an equable climate (e.g. Eberle et al., 2014; Eberle and Greenwood, 2012). However, recent analysis of carbon isotopes across tree rings within early-middle Eocene mummified wood has suggested three times as much precipitation fell within the summer season compared to winter (Schubert et al., 2012). Given the extreme winter darkness at such latitudes (e.g. Erberle and Greenwood, 2012), it is possible that proxies are not sensitive to the annual precipitation signal, but rather to a shorter, wetter growing season, especially because leaf size is thought to be a trade-off between maximising photosynthesis and minimising water loss (e.g. Peppe et al., 2011). Furthermore, the paleobotanic estimates included here support the concept of a " fossil climate" at high latitudes – i.e. a paleoclimatic state with no modern analogue, which compromises the application of the NLR concept and leaf area analysis, which are calibrated on climatic tolerances of modern-day vegetation distribution. Such an explanation is possible for the models that are cooler at the poles such as HadCM3L and that show a clear seasonal cycle in precipitation (Fig. 5); it is less convincing for those models that show a more equable distribution. There is, therefore, a need for further proxy studies which characterise high latitude precipitation regimes (e.g. Jahren and Sternberg, 2008; Jahren et al., 2009; Schubert et al., 2012). Nonetheless, current best estimates of early and mid Eocene precipitation rate provide independent evidence for a proxy-model anomaly at high latitudes.

5 Conclusions

The simulations within the EoMIP ensemble support an intensified hydrological cycle for the early Eocene, characterised by enhanced global mean precipitation and evaporation rates and increased meridional latent heat transport. The sensitivity of Eocene precipitation rates to warming is within the range suggested for future IPCC-style climate change scenarios, although some variation is introduced by models which incorporate additional feedbacks such as the TRIFFID simulations of Loptson et al. (2014). Differences in Eocene surface temperature distributions drive differences between models in their regional precipitation rates including for models with similar global precipitation sensitivities (dP/dT). Anomalies between simulations at high and low CO_2 may provide a way by which to constrain changes in precipitation occurring during hyperthermals (Winguth et al., 2010). Regions which are particularly different between HadCM3L and CCSM3 include coastal regions around the Peri-Tethys, the South Pacific, and tropical Africa which may represent targets for future proxy-data acquisition. We additionally show a summary of where the greatest model spread in some of the simulations of the EoMIP ensemble can be found, along with the existing paleobotanic precipitation estimates in Figure 12. This emphasises the need for additional data from the low latitudes in order to assess which models perform most realistically. There is now a need to move towards coordinated Eocene experiments between modelling groups which will improve the ability to mechanistically explain inter-model differences. Simulations with higher resolution 'state-of-the-art' GCMs would also be valuable, given the impacts that improved representation of orography and smaller scale atmospheric dynamics have had in reducing biases such as double ITCZ, representation of storm tracks and monsoon precipitation (Hack et al., 2006; Delworth et al., 2012; Gent et al., 2010).

Our proxy comparison emphasises the coupling between temperature and precipitation data-model anomalies. For high-latitude sites, model simulations are typically too cold, resulting in suppressed precipitation across a number of the models. Model simulations which enhance high-latitude warmth are in better agreement with existing proxy data, but the size of precipitation error bars prevents an identification of a "best" simulation. Models which warm the poles via high CO_2 (Liu et al., 2009; Winguth et al., 2010) are equally successful as models which achieve warmth at low CO_2 by varying poorly constrained parameter values (Sagoo et al., 2013; Kiehl and Shields, 2013). Better constraints on uncertain early Eocene boundary conditions, including CO_2, and more data from low latitudes are now required, as are other proxy approaches which can verify the high-latitude anomaly we have observed. Forward proxy modelling of water isotopes (Speelman et al., 2010; Sturm et al., 2009; Tindall et al., 2010) and comparison to archives which incorporate an Eocene δD or $\delta^{18}O$ signal (Zacke et al., 2009; Krishnan et al., 2014; Fricke and Wing, 2004) represents one such avenue. Given the potential for paleobotanic proxies to record a growing season signal in the high latitudes, alternative approaches to reconstructing precipitation seasonality are now needed (Schubert et al., 2012).

Proxies sensitive to hydrological changes offer an independent means to temperature by which to assess paleoclimatic model performance. Whilst elevated CO_2 causes a near-global increase in model-simulated surface temperatures, the same warming results in regions of both increased and reduced precipitation and $P-E$ within climate models (Figs. 5 and 9) Even without tightly constrained absolute changes in precipitation or net hydrological balance, the spatial pattern of qualitative indicators may prove a critical test of GCM ability for warm paleoclimates. Where estimates of absolute precipitation rates do exist, our preliminary model-data comparison indicates that GCMs are broadly unable to simulate sufficient high-latitude precipitation for the early Eocene, even with CO_2 configured at the upper end of proxy inferred estimates. Precipitation biases within models are coupled to those of temperature and our analysis is therefore consistent with the prevailing view of enhanced early Eocene high-latitude warmth. Our study represents a first step towards characterising the variability of the Eocene hydrological cycle simulated in GCMs. Further work is now required to study how other modelled aspects of the hydrological cycle such as runoff and salinity vary within the Eocene, and how these hydrological changes may relate to signals preserved in the geological record.

The Supplement related to this article is available online at doi:10.5194/cpd-11-3277-2015-supplement.

Acknowledgements

DJL acknowledges support through the NERC grant Cretaceous-Paleocene-Eocene: Exploring Climate and Climate Sensitivity (NE/K014757/1). RDP acknowledges the Royal Society for a Wolfson Research Merit Award. Finally, we thank two anonymous reviewers for their constructive comments which improved the quality of this manuscript.

References

Abbot, D. S. and Tziperman, E.: A high-latitude convective cloud feedback and equable climates, Q. J. Roy. Meteor. Soc., 134, 165–185, doi:10.1002/qj.211, 2008.

Akkiraz, M. S., Kayseri, M. S., and Akgun, F.: Palaeoecology of coal-bearing Eocene sediments in Central Anatolia (Turkey) based on quantitative palynological data, Turk. J. Earth Sci., 17, 317–360, 2008.

Allen, M. R. and Ingram, W. J.: Constraints on future changes in climate and the hydrologic cycle, Nature, 419, 224–232, doi:10.1038/nature01092, 2002.

Beerling, D. J., Fox, A., Stevenson, D. S., and Valdes, P. J.: Enhanced chemistry climate feedbacks in past greenhouse worlds, P. Natl. Acad. Sci. USA, 108, 9770–9775, doi:10.1073/pnas.1102409108, 2011.

Bice, K. L. and Marotzke, J.: Numerical evidence against reversed thermohaline circulation in the warm Paleocene/Eocene ocean, J. Geophys. Res.-Oceans, 106, 11529–11542,doi:10.1029/2000jc000561, 2001.

Bijl, P. K., Schouten, S., Sluijs, A., Reichart, G. J., Zachos, J. C., and Brinkhuis, H.: Early Palaeogene temperature evolution of the southwest Pacific Ocean, Nature, 461, 776–779, doi:10.1038/Nature08399, 2009.

Bolle, M. P. and Adatte, T.: Palaeocene early Eocene climatic evolution in the Tethyan realm: clay mineral evidence, Clay Miner., 36, 249–261, doi:10.1180/000985501750177979, 2001.

Bolle, M. P., Pardo, A., Adatte, T., Tantawy, A. A., Hinrichs, K. U., Von Salis, K., and Burns, S.: Climatic evolution on the southern and northern margins of the Tethys from the Paleocene to the early Eocene, GFF, 122, 31–32, doi:10.1080/11035890001221031, 2000.

Bony, S., Bellon, G., Klocke, D., Sherwood, S., Fermepin, S., & Denvil, S.: Robust direct effect of carbon dioxide on tropical circulation and regional precipitation, Nature Geoscience, 6, 447–451, doi:10.1038/ngeo1799, 2013

Bowen, G. J., Beerling, D. J., Koch, P. L., Zachos, J. C., and Quattlebaum, T.: A humid climate state during the Palaeocene/Eocene thermal maximum, Nature, 432, 495–499,doi:10.1038/Nature03115, 2004.

Braconnot, P., Harrison, S. P., Kageyama, M., Bartlein, P. J., Masson-Delmotte, V., Abe-Ouchi, A., Otto-Bliesner, B., and Zhao, Y.: Evaluation of climate models using palaeoclimatic data, Nature Climate Change, 2, 417–424, doi:10.1038/nclimate1456, 2012.

Brown, J. R., Power, S. B., Delage, F. P., Colman, R. a., Moise, A. F., & Murphy, B. F.: Evaluation of the South Pacific convergence zone in IPCC AR4 climate model simulations of the twentieth century, Journal of Climate, 24, 1565–1582, doi:10.1175/2010JCLI3942.1, 2011

Cai, W., Lengaigne, M., Borlace, S., Collins, M., Cowan, T., McPhaden, M. J., Timmermann, A., Power, S., Brown, J., Menkes, C., Ngari, A., Vincent, E.M., Widlansky, M. J.:More extreme swings of the South Pacific convergence zone due to greenhouse warming, Nature, 488, 365–369, doi:10.1038/nature11358, 2012

Chadwick, R., Boutle, I., & Martin, G.: Spatial Patterns of Precipitation Change in CMIP5: Why the Rich Do Not Get Richer in the Tropics, Journal of Climate, 26, 3803–3822, doi:10.1175/JCLI-D-12-00543.1, 2012

Chen, J. and Bordoni, S.: Intermodel spread of East Asian summer monsoon simulations in CMIP5, Geophys. Res. Lett., 41, 1314–1321, doi:10.1002/2013GL058981, 2014.

Chou, C., & Neelin, J. D.: Mechanisms of Global Warming Impacts on Regional Tropical Precipitation, Journal of Climate, 17(13), 2688–2701. doi:10.1175/1520-0442(2004)017<2688:MOGWIO>2.0.CO;2, 2014

Chou, C., Neelin, J. D., Chen, C. A., & Tu, J. Y., Evaluating the “rich-get-richer” mechanism in tropical precipitation change under global warming. Journal of Climate, 22, 1982–2005, doi:10.1175/2008JCLI2471.1, 2009

Clementz, M. T. and Sewall, J. O.: Latitudinal gradients in greenhouse seawater _18O: evidence from Eocene sirenian tooth enamel, Science, 332, 455–458, doi:10.1126/science.1201182,2011.

Collins, W. D., Bitz, C. M., Blackmon, M. L., Bonan, G. B., Bretherton, C. S., Carton, J. A.,Chang, P., Doney, S. C., Hack, J. J., Henderson, T. B., Kiehl, J. T., Large, W. G., McKenna, D.S ., Santer, B. D., and Smith, R. D.: The Community Climate System Model version 3 (CCSM3), J. Climate, 19, 2122–2143, doi:10.1175/JCLI-D-11-00290.1, 2006.

Contreras, L., Pross, J., Bijl, P. K., Koutsodendris, A., Raine, J. I., van de Schootbrugge, B.,and Brinkhuis, H.: Early to Middle Eocene vegetation dynamics at the Wilkes Land Margin (Antarctica), Rev. Palaeobot. Palyno., 197, 119–142, doi:10.1016/j.revpalbo.2013.05.009, 2013.

Cramer, B. S.: Orbital climate forcing of d13C excursions in the late Paleocene–early Eocene (chrons C24n–C25n), Paleoceanography, 18, 1–25, doi:10.1029/2003PA000909, 2003

Cox, P. M.: Description of the “ TRIFFID ” Dynamic Global Vegetation Model, Hadley Centre Technical Note, 24, 1–17, available at: http://www.metoffice.gov.uk/media/pdf/9/h/HCTN_24.pdf (last access: 16 July 2015), 2001.

Cox, P. M., Huntingford, C., and Harding, R. J.: A canopy conductance and photosynthesis model for use in a GCM land surface scheme, J. Hydrol., 212–213, 79–94, doi:10.1016/S0022-1694(98)00203-0, 1998.

Cox, P. M., Betts, R. A., Jones, C. D., Spall, S. A., and Totterdell, I. J.: Acceleration of global warming due to carbon-cycle feedbacks in a coupled climate model, Nature, 408, 184–187, doi:10.1038/35041539, 2000.

Dai, A.: Precipitation characteristics in eighteen coupled climate models, J. Climate, 19, 4605–4630, doi:10.1175/Jcli3884.1, 2006.

Dee, D. P., Uppala, S. M., Simmons, a. J., Berrisford, P., Poli, P., Kobayashi, S., Andrae, U., Balmaseda, M.A., Balsamo, G., Bauer, P., Bechtold, P., Beljaars, A.C.M., Van de Berg, L., Bidlot, J., Bormann, N., Delsol, C., Dragani, R., Fuentes, M., Geer, A.J., Haimberger, L., Healy, S.B., Hersbach, H., Hólm, E.V., Isaksen, L., Kållberg, P., Köhler, M., Matricardi, M., Mcnally, A.P., Monge-Sanz, B.M., Morcrette, J.J., Park, B.K., Peubey, C., de Rosnay, P., Tavolato, C., Thépaut, J.N., Vitart, F.: The ERA-Interim reanalysis: Configuration and performance of the data assimilation system, Quarterly Journal of the Royal Meteorological Society, 137, 553–597, doi:10.1002/qj.828, 2011.

Delworth, T. L., Rosati, A., Anderson, W., Adcroft, A. J., Balaji, V., Benson, R., Dixon, K., Griffies, S.M., Lee, H-C., Pacanowski, R.C., Vecchi, G.A., Wittenberg, A.T., Zeng, F., Zhang, R.: Simulated climate and climate change in the GFDL CM2.5 high-resolution coupled climate model, Journal of Climate, 25, 2755–2781, doi:10.1175/JCLI-D-11-00316.1, 2012

Douglas, P. M. J., Affek, H. P., Ivany, L. C., Houben, A. J. P., Sijp, W. P., Sluijs, A., Schouten, S., and Pagani, M.: Pronounced zonal heterogeneity in Eocene southern high-latitude sea surface temperatures, P. Natl. Acad. Sci. USA, 111, 6582–6587, doi:10.1073/pnas.1321441111, 2014.

Dunkley Jones, T., Lunt, D. J., Schmidt, D. N., Ridgwell, A., Sluijs, A., Valdes, P. J., and Maslin, M.: Climate model and proxy data constraints on ocean warming across the Paleocene–Eocene Thermal Maximum, Earth-Sci. Rev., 125, 123–145, doi:10.1016/j.earscirev.2013.07.004, 2013.

Eberle, J. J.: A new “tapir” from Ellesmere Island, Arctic Canada – implications for northern high latitude palaeobiogeography and tapir palaeobiology, Palaeogeogr. Palaeocl., 227, 311–322, doi:10.1016/j.palaeo.2005.06.008, 2005.

Eberle, J. J. and Greenwood, D. R.: Life at the top of the greenhouse Eocene world – a review of the Eocene flora and vertebrate fauna from Canada’s High Arctic, Geol. Soc. Am. Bull.,124, 3–23, doi:10.1130/B30571.1, 2012.

Eldrett, J. S., Greenwood, D. R., Harding, I. C., and Huber, M.: Increased seasonality through the Eocene to Oligocene transition in northern high latitudes, Nature, 459, 969–973, doi:10.1038/nature08069, 2009.

Eldrett, J. S., Greenwood, D. R., Polling, M., Brinkhuis, H., and Sluijs, A.: A seasonality trigger for carbon injection at the Paleocene–Eocene Thermal Maximum, Clim. Past, 10, 759–769, doi:10.5194/cp-10-759-2014, 2014.

Frakes, L. A.: Climates Throughout Geologic Time, Elsevier Scientific, Amsterdam, 310 pp.,1979.

Francis, J. E., Ashworth, A., Cantrill, D. J., Crame, J. A., Howe, J., Stephens, R., Tosolini, A.-M.,and Thorn, V.: 100 million years of Antarctic climate evolution: evidence from fossil plants, in: Antarctica: a Keystone in a Changing

World, Proceedings of the 10th International Symposium on Antarctic Earth Sciences, edited by: Cooper, A. K., Barrett, P. J., Stagg, H., Storey, E., Stump, E., Wise, W. and the 10th ISAES editorial team, The National Academies Press, Washington, DC, doi:10.3133/of2007-1047.kp03, 19–27, 2008.

Fricke, H. C. and Wing, S. L.: Oxygen isotope and paleobotanical estimates of temperature and _18O-latitude gradients over North America during the Early Eocene, Am. J. Sci., 304, 612–635, doi:10.2475/ajs.304.7.612, 2004.

Gasson, E., Lunt, D. J., DeConto, R., Goldner, A., Heinemann, M., Huber, M., LeGrande, A.N., Pollard, D., Sagoo, N., Siddall, M., Winguth, A., Valdes, P. J.: Uncertainties in the modelled CO2 threshold for Antarctic glaciation, Climate of the Past, 10(2), 451–466, doi:DOI 10.5194/cp-10-451-2014, 2014.

Gayó, E., Hinojosa, L. F., and Villagrán, C.: On the persistence of Tropical Paleofloras in central Chile during the Early Eocene, Rev. Palaeobot. Palyno., 137, 41–50, doi:10.1016/j.revpalbo.2005.09.001, 2005.

Gent, P., Yeager, S., Neale, R., Levis, S., & Bailey, D.: Improvements in a half degree atmosphere/land version of the CCSM, Climate Dynamics, 34(6), 819–833, doi:10.1007/s00382-009-0614-8, 2010

Golovneva, L. B.: Early Palaeogene floras of Spitsbergen and North Atlantic floristic exchange, Acta Universitatis Carolinae – Geologica, 44, 39–50, 2000.

Greenwood, D. R.: Eocene monsoon forests in central Australia?, Aust. Syst. Bot., 9, 95–112, doi:10.1071/Sb9960095, 1996.

Greenwood, D. R., Moss, P. T., Rowett, A. I., Vadala, A. J., and Keefe, R. L.: Plant communities and climate change in southeastern Australia during the early Paleogene, in: Causes and Consequences of Globally Warm Climates in the Early Paleogene, The Geological Society of America, Inc., Boulder, CO., doi:10.1130/0-8137-2369-8.365, 365–380, 2003.

Greenwood, D. R., Archibald, S. B., Mathewes, R. W., and Moss, P. T.: Fossil biotas from the Okanagan Highlands, southern British Columbia and northeastern Washington State: climates and ecosystems across an Eocene landscape, Can. J. Earth Sci., 42, 167–185, doi:10.1139/e04-100, 2005.

Greenwood, D. R., Basinger, J. F., and Smith, R. Y.: How wet was the Arctic Eocene rain forest? Estimates of precipitation from Paleogene Arctic macrofloras, Geology, 38, 15–18, doi:10.1130/G30218.1, 2010.

Grein, M., Utescher, T., Wilde, V., and Roth-Nebelsick, A.: Reconstruction of the middle Eocene climate of Messel using palaeobotanical data, Neues Jahrb. Geol. P.-A., 260, 305–318, 2011.

Greve, P., Orlowsky, B., Mueller, B., Sheffield, J., Reichstein, M., and Seneviratne, S. I.:Global assessment of trends in wetting and drying over land, Nat. Geosci., 7, 716–721, doi:10.1038/ngeo2247, 2014.

Gruber, A., Su, X. J., Kanamitsu, M., and Schemm, J.: The comparison of two merged rain gauge-satellite precipitation datasets, B. Am. Meteorol. Soc., 81, 2631–2644, doi:10.1175/1520-0477(2000)081<2631:Tcotmr>2.3.Co;2, 2000.

Hack, J. J., Caron, J. M., Danabasoglu, G., Oleson, K. W., Bitz, C., & Truesdale, J. E.: CCSM–CAM3 Climate Simulation Sensitivity to Changes in Horizontal Resolution, *Journal of Climate*, *19*, 2267–2289, doi:10.1175/JCLI3764.1, 2006

Hagemann, S., Arpe, K., and Roeckner, E.: Evaluation of the hydrological cycle in the ECHAM5 model, J. Climate, 19, 3810–3827, doi:10.1175/JCLI3831.1, 2006.

Handley, L., Pearson, P. N., McMillan, I. K., and Pancost, R. D.: Large terrestrial and marine carbon and hydrogen isotope excursions in a new Paleocene/Eocene boundary section from Tanzania, Earth Planet. Sc. Lett., 275, 17–25, doi:10.1016/j.epsl.2008.07.030, 2008.

Handley, L., Crouch, E. M., and Pancost, R. D.: A New Zealand record of sea level rise and environmental change during the Paleocene–Eocene Thermal Maximum, Palaeogeogr. Palaeocl., 305, 185–200, doi:10.1016/j.palaeo.2011.03.001, 2011.

Handley, L., O'Halloran, A., Pearson, P. N., Hawkins, E., Nicholas, C. J., Schouten, S., McMillan, I. K., and Pancost, R. D.: Changes in the hydrological cycle in tropical East Africa during the Paleocene–Eocene Thermal Maximum, Palaeogeogr. Palaeocl., 329, 10–21,doi:10.1016/j.palaeo.2012.02.002, 2012.

Heinemann, M., Jungclaus, J. H., and Marotzke, J.: Warm Paleocene/Eocene climate as simulated in ECHAM5/MPIOM, Clim. Past, 5, 785–802, doi:10.5194/cp-5-785-2009, 2009.

Held, I. M. and Soden, B. J.: Robust responses of the hydrological cycle to global warming, J. Climate, 19, 5686–5699, doi:10.1175/JCLI3990.1, 2006.

Hinojosa, L. F. and Villagrán, C.: Did South American Mixed Paleofloras evolve under thermal equability or in the absence of an effective Andean barrier during the Cenozoic?, Palaeogeogr. Palaeocl., 217, 1–23, doi:10.1016/j.palaeo.2004.11.013, 2005.

Hinojosa, L. F., Pesce, O., Yabe, A., Uemura, K., and Nishida, H.: physiognomical analysis and paleoclimate of the Ligorio Márquez fossil flora, Ligorio Márquez formation, 46_450 S, Chile, in: Post-Cretaceous Floristic Changes in Southern Patagonia, Chile, edited by: Nishida, H.,ChuoUniv., Tokyo, 45–55, 2006.

Hollis, C. J., Taylor, K. W. R., Handley, L., Pancost, R. D., Huber, M., Creech, J. B., Hines, B. R., Crouch, E. M., Morgans, H. E. G., Crampton, J. S., Gibbs, S., Pearson, P. N., and Zachos, J. C.: Early Paleogene temperature history of the Southwest Pacific Ocean: reconciling proxies and models, Earth Planet. Sc. Lett., 349, 53–66, doi:10.1016/j.epsl.2012.06.024, 2012.

Huber, M.: Climate change. A hotter greenhouse?, Science, 321, 353–354, doi:10.1126/science.1161170, 2008.

Huber, M., Brinkhuis, H., Stickley, C. E., Döös, K., Sluijs, A., Warnaar, J., Schellenberg, S.A., Williams, G. L.: Eocene circulation of the Southern Ocean: Was Antarctica kept warm by subtropical waters?, Paleoceanography, 19, 1–12, doi:10.1029/2004PA001014, 2004.
Huber, M. and Caballero, R.: The early Eocene equable climate problem revisited, Clim. Past, 7, 603–633, doi:10.5194/cp-7-603-2011, 2011.
Huber, M. and Goldner, A.: Eocene monsoons, J. Asian Earth Sci., 44, 3–23, doi:10.1016/j.jseaes.2011.09.014, 2012.
Huber, M. and Sloan, L. C.: Heat transport, deep waters, and thermal gradients: coupled simulation of an Eocene greenhouse climate, Geophys. Res. Lett., 28, 3481–3484, doi:10.1029/2001GL012943, 2001.
Hunt, R. J. and Poole, I.: Paleogene West Antarctic climate and vegetation history in light of new data from King George Island, Geol. S. Am. S., 369, 395–412, doi:10.1130/0-8137- 2369-8.395, 2003.
Inglis, G.N., Farnsworth, A., Lunt, D., Foster, G.L., Hollis, C.J., Pagani, M., Jardine, P., Pearson, P.N., Markwick, P., Galsworthy, A., Raynham, A., Taylor, K.W.R. and Pancost, R.D.: Descent towards the Icehouse: Eocene sea surface cooling inferred from GDGT distributions, Paleoceanography, 30, 1000 – 1020, doi: 10.1002/2014PA002723, 2015
Jacobs, B. F. and Herendeen, P. S.: Eocene dry climate and woodland vegetation in tropical Africa reconstructed from fossil leaves from northern Tanzania, Palaeogeogr. Palaeocl., 213,115–123, doi:10.1016/j.palaeo.2004.07.007, 2004.
Jacques, F. M. B., Shi, G., Li, H., and Wang, W.: An early-middle Eocene Antarctic summer monsoon: evidence of "fossil climates", Gondwana Res., 25, 1422–1428, doi:10.1016/j.gr.2012.08.007, 2014.
Joetzjer, E., Douville, H., Delire, C., & Ciais, P.: Present-day and future Amazonian precipitation in global climate models: CMIP5 versus CMIP3, Climate Dynamics, 41, 2921–2936, doi:10.1007/s00382-012-1644-1, 2013
John, C. M., Bohaty, S. M., Zachos, J. C., Sluijs, A., Gibbs, S., Brinkhuis, H., and Bralower, T. J.: North American continental margin records of the Paleocene–Eocene thermal maximum: implications for global carbon and hydrological cycling, Paleoceanography, 23, Pa2217, doi:10.1029/2007pa001465, 2008.
John, C. M., Banerjee, N. R., Longstaffe, F. J., Sica, C., Law, K. R., and Zachos, J. C.: Clay assemblage and oxygen isotopic constraints on the weathering response to the Paleocene–Eocene thermal maximum, east coast of North America, Geology, 40, 591–594, doi:10.1130/G32785.1, 2012.
Jones, C., Gregory, J., Thorpe, R., Cox, P., Murphy, J., Sexton, D., and Valdes, P.: Systematic optimisation and climate simulation of FAMOUS, a fast version of HadCM3, Clim. Dynam., 25, 189–204, doi:10.1007/s00382-005-0027-2, 2005.
Kaiser, T. M., Ansorge, J., Arratia, G., Bullwinkel, V., Gunnell, G. F., Herendeen, P. S., Jacobs, B., Mingram, J., Msuya, C., Musolff, A., Naumann, R., Schulz, E., and Wilke, V.: The maar lake of Mahenge (Tanzania) – unique evidence of Eocene terrestrial environments in sub-Sahara Africa, Z. Dtsch. Ges. Geowiss., 157, 411–413, 2006.
Kender, S., Stephenson, M. H., Riding, J. B., Leng, M. J., Knox, R. W. O. B., Peck, V. L., Kendrick, C. P., Ellis, M. A., Vane, C. H., and Jamieson, R.: Marine and terrestrial environmental changes in NW Europe preceding carbon release at the Paleocene–Eocene transition, Earth Planet. Sc. Lett., 353–354, 108–120, doi:10.1016/j.epsl.2012.08.011, 2012.
Kiehl, J. T. and Shields, C. A.: Sensitivity of the Palaeocene–Eocene Thermal Maximum climate to cloud properties, Philos. T. R. Soc. A, 371, 20130093, doi:10.1098/Rsta.2013.0093, 2013.
Kirk-Davidoff, D. B.: On the feedback of stratospheric clouds on polar climate, Geophysical Research Letters, 29, 1–4, doi:10.1029/2002GL014659, 2002.
Kirtland Turner, S., Sexton, P. F., Charles, C. D., & Norris, R. D.: Persistence of carbon release events through the peak of early Eocene global warmth, Nature Geosci, 7(10), 748–751, Retrieved from http://dx.doi.org/10.1038/ngeo2240, 2014.
Komar, N., Zeebe, R. E., & Dickens, G. R., Understanding long-term carbon cycle trends: The late Paleocene through the early Eocene, Paleoceanography, 28, 650–662. doi:10.1002/palo.20060, 2013
Korty, R. L., Emanuel, K. a., & Scott, J. R.: Tropical cyclone-induced upper-ocean mixing and climate: Application to equable climates, Journal of Climate, 21, 638–654, doi:10.1175/2007JCLI1659.1, 2008.
Knutti, R. and Sedlacek, J.: Robustness and uncertainties in the new CMIP5 climate model projections, Nature Climate Change, 3, 369–373, doi:10.1038/Nclimate1716, 2013.
Kraus, M. J., McInerney, F. A., Wing, S. L., Secord, R., Baczynski, A. A., and Bloch, J. I.: Paleohydrologic response to continental warming during the Paleocene– Eocene Thermal Maximum, Bighorn Basin, Wyoming, Palaeogeogr. Palaeocl., 370, 196–208, doi:10.1016/j.palaeo.2012.12.008, 2013.
Krishnan, S., Pagani, M., Huber, M., and Sluijs, A.: High latitude hydrological changes during the Eocene Thermal Maximum 2, Earth Planet. Sc. Lett., 404, 167–177, doi:10.1016/j.epsl.2014.07.029, 2014.
Kump, L. R. and Pollard, D.: Amplification of Cretaceous warmth by biological cloud feedbacks, Science, 320, 195, doi:10.1126/science.1153883, 2008.
Legates, D. R. and Willmott, C. J.: Mean seasonal and spatial variability in gauge-corrected, global precipitation, Int. J. Climatol., 10, 111–127, doi:10.1002/joc.3370100202, 1990.

Licht, A., van Cappelle, M., Abels, H. A., Ladant, J.-B., Trabucho-Alexandre, J., France-Lanord, C., Donnadieu, Y., Vandenberghe, J., Rigaudier, T., Lecuyer, C., Terry Jr, D., Adriaens, R., Boura, A., Guo, Z., Soe, A. N., Quade, J., Dupont-Nivet, G., Jaeger, J.-J., and Jaeger, J.-J.: Asian monsoons in a late Eocene greenhouse world, Nature, 513, 501–506, doi:10.1038/nature13704, 2014.

Lin, J-L. L.: The double-ITCZ problem in IPCC AR4 coupled GCMs: Ocean-atmosphere feedback analysis, Journal of Climate, 20, 4497–4525, doi:10.1175/JCLI4272.1, 2007

Littler, K., Röhl, U., Westerhold, T., & Zachos, J. C.: A high-resolution benthic stable-isotope record for the South Atlantic: Implications for orbital-scale changes in Late Paleocene-Early Eocene climate and carbon cycling, Earth and Planetary Science Letters, 401, 18–30, doi:10.1016/j.epsl.2014.05.054, 2014

Liu, C., Allan, R. P., Brooks, M., & Milton, S.: Comparing tropical precipitation simulated by the Met Office NWP and climate models with satellite observations, Journal of Applied Meteorology and Climatology, 53, 200–214, doi:10.1175/JAMC-D-13-082.1, 2014

Liu, Z., Pagani, M., Zinniker, D., Deconto, R., Huber, M., Brinkhuis, H., Shah, S. R., Leckie, R. M., and Pearson, A.: Global cooling during the eocene-oligocene climate transition, Science, 323, 1187–1190, doi:10.1126/science.1166368, 2009.

Loptson, C. A., Lunt, D. J., and Francis, J. E.: Investigating vegetation–climate feedbacks during the early Eocene, Clim. Past, 10, 419–436, doi:10.5194/cp-10-419-2014, 2014.

Lourens, L., Sluijs, A., Kroon, D., Zachos, J. C., Thomas, E., Röhl, U., Bowles, J., Raffi, I.: Astronomical pacing of late Palaeocene to early Eocene global warming events. Nature, 435, 1083–1087, doi:10.1038/nature03814, 2005

Lowenstein, T. K. and Demicco, R. V.: Elevated Eocene atmospheric CO2 and its subsequent decline, Science, 313, 1928, doi:10.1126/science.1129555, 2006.

Lunt, D. J., Valdes, P. J., Jones, T. D., Ridgwell, A., Haywood, A. M., Schmidt, D. N., Marsh, R., and Maslin, M.: CO2-driven ocean circulation changes as an amplifier of Paleocene–Eocene Thermal Maximum hydrate destabilization, Geology, 38, 875–878, doi:10.1130/G31184.1, 2010.

Lunt, D. J., Dunkley Jones, T., Heinemann, M., Huber, M., LeGrande, A., Winguth, A., Loptson, C., Marotzke, J., Roberts, C. D., Tindall, J., Valdes, P., and Winguth, C.: A model–data comparison for a multi-model ensemble of early Eocene atmosphere–ocean simulations: EoMIP, Clim. Past, 8, 1717–1736, doi:10.5194/cp-8-1717-2012, 2012.

Lunt, D. J., Farnsworth, A., Loptson, C., Foster, G. L., Markwick, P., O'Brien, C. L., Pancost, R. D., Robinson, S. A., and Wrobel, N.: Palaeogeographic controls on climate and proxy interpretation, Clim. Past Discuss., 11, 5683-5725, doi:10.5194/cpd-11-5683-2015, 2015.

Markwick, P. J.: Fossil crocodilians as indicators of Late Cretaceous and Cenozoic climates: implications for using palaeontological data in reconstructing palaeoclimate, Palaeogeogr. Palaeocl., 137, 205–271, doi:10.1016/S0031-0182(97)00108-9, 1998.

Matthews, A. J.: A multiscale framework for the origin and variability of the South Pacific Convergence Zone, Quarterly Journal of the Royal Meteorological Society, 138(666), 1165–1178, doi:10.1002/qj.1870, 2012

McInerney, F. a., & Wing, S. L.: The Paleocene-Eocene Thermal Maximum: A Perturbation of Carbon Cycle, Climate, and Biosphere with Implications for the Future, Annual Review of Earth and Planetary Sciences, 39, 489–516, doi:10.1146/annurev-earth-040610-133431, 2011.

Mehran, A., AghaKouchak, A., & Phillips, T. J.: Evaluation of CMIP5 continental precipitation simulations relative to satellite-based gauge-adjusted observations, Journal of Geophysical Research, 1–17, doi:10.1002/2013JD021272, 2014

Mosbrugger, V. and Utescher, T.: The coexistence approach – a method for quantitative reconstructions of Tertiary terrestrial palaeoclimate data using plant fossils, Palaeogeogr. Palaeocl., 134, 61–86, doi:10.1016/S0031-0182(96)00154-X, 1997.

Mosbrugger, V., Utescher, T., and Dilcher, D. L.: Cenozoic continental climatic evolution of Central Europe, P. Natl. Acad. Sci. USA, 102, 14964–14969, doi:10.1073/pnas.0505267102, 2005.

Nicolo, M. J., Dickens, G. R., Hollis, C. J., & Zachos, J. C.: Multiple early Eocene hyperthermals: Their sedimentary expression on the New Zealand continental margin and in the deep sea, Geology, 35, 699–702, doi:10.1130/G23648A.1, 2007

Oleson, K. W., Dai, Y., Bonan, G. B., Bosilovich, M., Dickinson, R. E., Dirmeyer, P., Hoffman, F., Houser, P., Levis, S., Niu, G.-Y., Thornton, P., Vertenstein, M., Yang, Z.-L., and Zeng, X. : Technical Description of the Community Land Model (CLM), NCAR Technical Note, NCAR/TN-46, 186, Boulder, CO., doi:10.5065/D6N877R0, 2004.

Pagani, M., Pedentchouk, N., Huber, M., Sluijs, A., Schouten, S., Brinkhuis, H., Sinninghe Damsté, J. S., and Dickens, G. R.: Arctic hydrology during global warming at the Palaeocene/Eocene Thermal Maximum, Nature, 442, 671–675, doi:10.1038/Nature05043, 2006.

Pagani, M., Huber, M., and Sageman, B.: Greenhouse climates, in: Treatise on Geochemistry, 2nd edn., Vol. 6, 281–304, Elsevier Ltd. Amsterdam, doi:10.1016/B978-0-08-095975-7.01314-0, 2013.

Pancost, R. D., Taylor, K. W. R., Inglis, G. N., Kennedy, E. M., Handley, L., Hollis, C. J., Crouch, E. M., Pross, J., Huber, M., Schouten, S., Pearson, P. N., Morgans, H. E. G., and Raine, J. I.: Early Paleogene evolution of terrestrial climate in the SW Pacific, Southern New Zealand, Geochem. Geophy. Geosy., 14, 5413–5429, doi:10.1002/2013gc004935, 2013.

Pearson, P. N., van Dongen, B. E., Nicholas, C. J., Pancost, R. D., Schouten, S., Singano, J. M., and Wade, B. S.: Stable warm tropical climate through the Eocene Epoch, Geology, 35, 211–214, doi:10.1130/G23175A.1, 2007.

Peppe, D. J., Royer, D. L., Cariglino, B., Oliver, S. Y., Newman, S., Leight, E., Enikolopov, G., Fernandez-Burgos, M., Herrera, F., Adams, J.M., Correa, E., Currano, E. D., Erickson, J. M., Hinojosa, L. F., Hoganson, J. W., Iglesias, A., Jaramillo, C. A., Johnson, K. R., Jordan, G. J., Kraft, N. J. B., Lovelock, E. C., Lusk, C. H., Niinemets, Ü., Peñuelas, J., Rapson, G., Wing, S. L., and Wright, I. J.: Sensitivity of leaf size and shape to climate: global patterns and paleoclimatic applications, New Phytol., 190, 724–739, doi:10.1111/j.1469-8137.2010.03615.x, 2011.

Phillips, T. J., & Gleckler, P. J.: Evaluation of continental precipitation in 20th century climate simulations: The utility of multimodel statistics, Water Resources Research, 42, W03202. doi:10.1029/2005WR004313, 2006

Pierrehumbert, R. T.: The hydrologic cycle in deep-time climate problems, Nature, 419, 191–198, 2002.

Poole, I., Cantrill, D., and Utescher, T.: A multi-proxy approach to determine Antarctic terrestrial palaeoclimate during the Late Cretaceous and Early Tertiary, Palaeogeogr. Palaeocl., 222, 95–121, doi:10.1016/j.palaeo.2005.03.011, 2005.

Pross, J., Contreras, L., Bijl, P. K., Greenwood, D. R., Bohaty, S. M., Schouten, S., Bendle, J. A., Rohl, U., Tauxe, L., Raine, J. I., Huck, C. E., van de Flierdt, T., Jamieson, S. S. R., Stickley, C. E., van de Schootbrugge, B., Escutia, C., Brinkhuis, H., and IODP Expedition 318 Scientists: Persistent near-tropical warmth on the Antarctic continent during the early Eocene epoch, Nature, 488, 73–77, doi:10.1038/Nature11300, 2012.

Quan, C., Liu, Y. S. C., and Utescher, T.: Eocene monsoon prevalence over China: a paleobotanical perspective, Palaeogeogr. Palaeocl., 365–366, 302–311, doi:10.1016/j.palaeo.2012.09.035, 2012.

Randall, D. A., Wood, R. A., Bony, S., Colman, R., Fichefet, T., Fyfe, J., Kattsov, V., Pitman, A., Shukla, J., Srinivasan, J., Stouffer, R. J., Sumi, A., and Taylor, K. E. : Climate models and their evaluation, in: Climate Change 2007: the Physical Science Basis. Contribution of Working Group I to the Fourth Assessment Report of the Intergovernmental Panel on Climate Change, Cambridge University Press, NY, 591–662, 2007.

Robert, C. and Kennett, J. P.: Antarctic subtropical humid episode at the Paleocene–Eocene boundary: clay-mineral evidence, Geology, 22, 211–214, doi:10.1130/0091-7613(1994)022<0211:Asheat>2.3.Co;2, 1994.

Roberts, C. D., LeGrande, A. N., and Tripati, A. K.: Climate sensitivity to Arctic seaway restriction during the early Paleogene, Earth Planet. Sc. Lett., 286, 576–585, doi:10.1016/j.epsl.2009.07.026, 2009.

Roeckner, E., Bäuml, G., Bonaventura, L., Brokopf, R., Esch, M., Giorgetta, M., Hagemann, S., Kirchner, I., Kornblueh, L., Rhodin, A., Schlese, U., Schulzweida, U., and Tompkins, A.:The atmospheric general circulation model ECHAM5: Part 1: Model description, Deutsches Klimarechenzentrum, Vol. 349, 1–140, available at: https://www.mpimet.mpg.de/fileadmin/publikationen/Reports/max_scirep_349.pdf (last access: 16 July 2015), 2003.

Royer, D. L., Wing, S. L., Beerling, D. J., Jolley, D.W., Koch, P. L., Hickey, L. J., and Berner, R. A.: Paleobotanical evidence for near present-day levels of atmospheric CO2 during part of the tertiary, Science, 292, 2310–2313, doi:10.1126/science.292.5525.2310, 2001.

Royer, D. L., Wilf, P., Janesko, D. A., Kowalski, E. A., and Dilcher, D. L.: Correlations of climate and plant ecology to leaf size and shape: potential proxies for the fossil record, Am. J. Bot., 92, 1141–1151, doi:10.3732/ajb.92.7.1141, 2005.

Royer, D. L., Sack, L., Wilf, P., Lusk, C. H., Jordan, G. J., Niinemets, Ü., Wright, I. J., Westoby, M., Cariglino, B., Coley, P. D., Cutter, A. D., Johnson, K. R., Labandeira, C. C., Moles, A. T., Palmer, M. B., and Valladares, F.: Fossil leaf economics quantified: calibration, Eocene case study, and implications, Paleobiology, 33, 574–589, doi:10.1666/07001.1, 2007.

Sagoo, N., Valdes, P., Flecker, R., and Gregoire, L. J.: The Early Eocene equable climate problem: can perturbations of climate model parameters identify possible solutions?, Philos. T. R. Soc. A, 371, 20130123, doi:10.1098/Rsta.2013.0123, 2013.

Schmidt, G. A., Ruedy, R., Hansen, J. E., Aleinov, I., Bell, N., Bauer, M., Bauer, S., Cairns, B., Canuto, V., Cheng, Y., Del Genio, A., Faluvegi, G., Friend, A. D., Hall, T. M., Hu, Y., Kelley, M., Kiang, N. Y., Koch, D., Lacis, A. A., Lerner, J., Lo, K. K., Miller, R. L., Nazarenko, L., Oinas, V., Perlwitz, J., Perlwitz, J., Rind, D., Romanou, A., Russell, G. L., Sato, M., Shindell, D. T., Stone, P. H., Sun, S., Tausnev, N., Thresher, D., and Yao, M. S.: Present-day atmospheric simulations using GISS ModelE: comparison to in situ, satellite, and reanalysis data, J. Climate, 19, 153–192, doi:10.1175/JCLI3612.1, 2006.

Schmitz, B. and Pujalte, V.: Abrupt increase in seasonal extreme precipitation at the Paleocene–Eocene boundary, Geology, 35, 215–218, doi:10.1130/G23261a.1, 2007.

Schubert, B. A., Jahren, A. H., Eberle, J. J., Sternberg, L. S. L., and Eberth, D. A.: A summertime rainy season in the Arctic forests of the Eocene, Geology, 40, 523–526, doi:10.1130/G32856.1, 2012.

Sewall, J. O., Sloan, L. C., Huber, M., and Wing, S.: Climate sensitivity to changes in land surface characteristics, Global Planet. Change, 26, 445–465, doi:10.1016/S0921-8181(00)00056-4, 2000.

Shellito, C. J. and Sloan, L. C.: Reconstructing a lost Eocene Paradise, Part II: On the utility of dynamic global vegetation models in pre-Quaternary climate studies, Global Planet. Change, 50, 18–32, doi:10.1016/j.gloplacha.2005.08.002, 2006.

Shellito, C. J., Lamarque, J. F., and Sloan, L. C.: Early Eocene Arctic climate sensitivity to *p*CO2 and basin geography, Geophys. Res. Lett., 36, L09707, doi:10.1029/2009gl037248, 2009.

Sloan, L. C., Walker, J. C., Moore, T. C., Rea, D. K., and Zachos, J. C.: Possible methane induced polar warming in the early Eocene, Nature, 357, 320–322, doi:10.1038/357320a0,1992.

Slotnick, B. S., Dickens, G. R., Nicolo, M. J., Hollis, C. J., Crampton, J. S., Zachos, J. C., & Sluijs, A.: Large-Amplitude Variations in Carbon Cycling and Terrestrial Weathering during the Latest Paleocene and Earliest Eocene: The Record at Mead Stream, New Zealand, The Journal of Geology, 120, 487–505, doi:10.1086/666743, 2012

Sluijs, A., Schouten, S., Pagani, M., Woltering, M., Brinkhuis, H., Damste, J. S. S., Dickens, G. R., Huber, M., Reichart, G. J., Stein, R., Matthiessen, J., Lourens, L. J., Pedentchouk, N., Backman, J., Moran, K., and Expedition 302 Scientists: Subtropical arctic ocean temperatures during the Palaeocene/Eocene thermal maximum, Nature, 441, 610– 613, doi:10.1038/Nature04668, 2006.

Sluijs, A., Bowen, G. J., Brinkhuis, H., Lourens, L. J., and Thomas, E.: The Palaeocene-Eocene Thermal Maximum super greenhouse: biotic and geochemical signatures, age models and mechanisms of global change, in: Deep-Time Perspectives on Climate Change: Marrying the Signal from Computer Models and Biological Proxies, edited by: Williams, M., Haywood, A. M., Gregory, F. J., and Schmidt, D. N., The Geological Society, Bath, 323–350, 2007.

Sluijs, A., Schouten, S., Donders, T. H., Schoon, P. L., Röhl, U., Reichart, G., Sangiorgi, F., Kim, J-H., Damsté, J. S. S.: Warm and wet conditions in the Arctic region during Eocene Thermal Maximum 2, Nature Geoscience, 2, 777–780, doi:10.1038/NGEO668, 2009

Smith, F., Wing, S., and Freeman, K.: Magnitude of the carbon isotope excursion at the Paleocene–Eocene thermal maximum: the role of plant community change, Earth Planet. Sc. Lett., 262, 50–65, doi:10.1016/j.epsl.2007.07.021, 2007.

Smith, R. S. and Gregory, J.: The last glacial cycle: transient simulations with an AOGCM, Clim. Dynam., 38, 1545–1559, doi:10.1007/s00382-011-1283-y, 2012.

Smith, R. S., Gregory, J. M., and Osprey, A.: A description of the FAMOUS (version XDBUA) climate model and control run, Geosci. Model Dev., 1, 53–68, doi:10.5194/gmd-1-53-2008, 2008.

Smith, R. Y., Greenwood, D. R., and Basinger, J. F.: Estimating paleoatmospheric *p*CO2 during the Early Eocene Climatic Optimum from stomatal frequency of Ginkgo, Okanagan Highlands, British Columbia, Canada, Palaeogeogr. Palaeocl., 293, 120–131, doi:10.1016/j.palaeo.2010.05.006, 2010.

Smith, R. Y., Basinger, J. F., and Greenwood, D. R.: Early Eocene plant diversity and dynamics in the Falkland flora, Okanagan Highlands, British Columbia, Canada, Palaeobiodiversity and Palaeoenvironments, 92, 309–328, doi:10.1007/s12549-011-0061-5, 2012.

Speelman, E. N., Sewall, J. O., Noone, D., Huber, M., von der Heydt, A., Damste, J. S., and Reichart, G. J.: Modeling the influence of a reduced equator-to-pole sea surface temperature gradient on the distribution of water isotopes in the Early/Middle Eocene, Earth Planet. Sc. Lett., 298, 57–65, doi:10.1016/j.epsl.2010.07.026, 2010.

Stap, L., Lourens, L. J., Thomas, E., Sluijs, A., Bohaty, S., & Zachos, J. C.: High-resolution deep-sea carbon and oxygen isotope records of Eocene Thermal Maximum 2 and H2, Geology, 38, 607–610, doi:10.1130/G30777.1, 2010

Sturm, C., Zhang, Q., and Noone, D.: An introduction to stable water isotopes in climate models: benefits of forward proxy modelling for paleoclimatology, Clim. Past, 6, 115–129, doi:10.5194/cp-6-115-2010, 2010.

Suarez, M. B., Gonzalez, L. A., Ludvigson, G. A., Vega, F. J., and Alvarado-Ortega, J.: Isotopic composition of low-latitude paleoprecipitation during the Early Cretaceous, Geol. Soc. Am. Bull., 121, 1584–1595, doi:10.1130/B26453.1, 2009.

Sun, X. and Wang, P.: How old is the Asian monsoon system? – Palaeobotanical records from China, Palaeogeogr. Palaeocl., 222, 181–222, doi:10.1016/j.palaeo.2005.03.005, 2005.

Sunderlin, D., Loope, G., Parker, N. E., and Williams, C. J.: Paleoclimatic and paleoecological implications of a Paleocene–Eocene fossil leaf assemblage, Chickaloon Formation, Alaska, Palaios, 26, 335–345, doi:10.2110/palo.2010.p10-077r, 2011.

Sunderlin, D., Trop, J. M., Idleman, B. D., Brannick, A., White, J. G., and Grande, L.: Paleoenvironment and paleoecology of a Late Paleocene high-latitude terrestrial succession, Arkose Ridge Formation at Box Canyon, southern Talkeetna Mountains, Alaska, Palaeogeogr. Palaeocl., 401, 57–80, doi:10.1016/j.palaeo.2014.02.012, 2014.

Taylor, K. E., Stouffer, R. J., and Meehl, G. A.: An overview of CMIP5 and the experiment design, B. Am. Meteorol. Soc., 93, 485–498, doi:10.1175/BAMS-D-11-00094.1, 2012.

Taylor, K. W. R., Huber, M., Hollis, C. J., Hernandez-Sanchez, M. T., and Pancost, R. D.: Reevaluating modern and Palaeogene GDGT distributions: implications for SST reconstructions, Global Planet. Change, 108, 158–174, doi:10.1016/j.gloplacha.2013.06.011, 2013.

Tindall, J., Flecker, R., Valdes, P., Schmidt, D. N., Markwick, P., and Harris, J.: Modelling the oxygen isotope distribution of ancient seawater using a coupled ocean–atmosphere GCM: implications for reconstructing early Eocene climate, Earth Planet. Sc. Lett., 292, 265–273, doi:10.1016/j.epsl.2009.12.049, 2010.
Tipple, B. J., Berke, M. A., Doman, C. E., Khachaturyan, S., and Ehleringer, J. R.: Leaf-wax n-alkanes record the plant–water environment at leaf flush, P. Natl. Acad. Sci. USA, 110, 2659–2664, doi:10.1073/pnas.1213875110, 2013.
Trenberth, K. E.: Changes in precipitation with climate change, Clim. Res., 47, 123–138, doi:10.3354/cr00953, 2011.
Turner, A. G. and Slingo, J. M.: Uncertainties in future projections of extreme precipitation in the Indian monsoon region, Atmos. Sci. Lett., 10, 152–158, doi:10.1002/asl.223, 2009.
Uhl, D., Traiser, C., Griesser, U., and Denk, T.: Fossil leaves as palaeoclimate proxies in the Palaeogene of Spitsbergen (Svalbard), Acta Palaeobotanica, 47, 89–107, 2007.
Valdes, P.: Built for stability, Nat. Geosci., 4, 414–416, doi:10.1038/ngeo1200, 2011.
Waddell, L. M. and Moore, T. C.: Salinity of the Eocene Arctic Ocean from oxygen isotope analysis of fish bone carbonate, Paleoceanography, 23, PA1S12, doi:10.1029/2007PA001451, 2008.
Wang, D., Lu, S., Han, S., Sun, X., and Quan, C.: Eocene prevalence of monsoon-like climate over eastern China reflected by hydrological dynamics, J. Asian Earth Sci., 62, 776–787, doi:10.1016/j.jseaes.2012.11.032, 2013.
White, T., Gonzalez, L., Ludvigson, G., and Poulsen, C.: Middle Cretaceous greenhouse hydrologic cycle of North America, Geology, 29, 363–366, doi:10.1130/0091-7613(2001)029<0363:Mcghco>2.0.Co;2, 2001.
Wilf, P.: Late Paleocene–Early Eocene climate changes in southwestern Wyoming: paleobotanical analysis, Geol. Soc. Am. Bull., 112, 292–307, doi:10.1130/0016-7606(2000)112<0292:Lpeecc>2.3.Co;2, 2000.
Wilf, P., Wing, S. L., Greenwood, D. R., and Greenwood, C. L.: Using fossil leaves as paleoprecipitation indicators: an Eocene example, Geology, 26, 203–206, doi:10.1130/0091-7613(1998)026<0203:UFLAPI>2.3.Co;2, 1998.
Wilf, P., Johnson, K. R., Cuneo, N. R., Smith, M. E., Singer, B. S., and Gandolfo, M. A.: Eocene plant diversity at Laguna del Hunco and Rio Pichileufu, Patagonia, Argentina, Am. Nat., 165, 634–650, doi:10.1086/430055, 2005.
Williams, J. H. T., Smith, R. S., Valdes, P. J., Booth, B. B. B., and Osprey, A.: Optimising the FAMOUS climate model: inclusion of global carbon cycling, Geosci. Model Dev., 6, 141–160, doi:10.5194/gmd-6-141-2013, 2013.
Wing, S. L. and Greenwood, D. R.: Fossils and fossil climate – the case for equable continental interiors in the Eocene, Philos. T. Roy. Soc. B, 341, 243–252, doi:10.1098/rstb.1993.0109, 1993.
Wing, S. L., Harrington, G. J., Smith, F. A., Bloch, J. I., Boyer, D. M., and Freeman, K. H.: Transient floral change and rapid global warming at the Paleocene–Eocene boundary, Science, 310, 993–996, doi:10.1126/science.1116913, 2005.
Wing, S. L., Herrera, F., Jaramillo, C. A., Gómez-Navarro, C., Wilf, P., and Labandeira, C. C.: Late Paleocene fossils from the Cerrejon Formation, Colombia, are the earliest record of Neotropical rainforest, P. Natl. Acad. Sci. USA, 106, 18627–18632, doi:10.1073/pnas.0905130106, 2009.
Winguth, A., Shellito, C., Shields, C., and Winguth, C.: Climate response at the Paleocene–Eocene Thermal Maximum to greenhouse gas forcing – a model study with CCSM3, J. Climate, 23, 2562–2584, doi:10.1175/2009jcli3113.1, 2010.
Winguth, A. M. E., Thomas, E., and Winguth, C.: Global decline in ocean ventilation, oxygenation, and productivity during the Paleocene–Eocene Thermal Maximum: implications for the benthic extinction, Geology, 40, 263–266, doi:10.1130/G32529.1, 2012.
Wolfe, J. A.: A method of obtaining climatic parameters from leaf assemblages, US Geological Survey Bulletin, United States Government Printing Office, Washington, 2040, 1–71, 1993.
Yapp, C. J.: Fe(CO3)OH in goethite from a mid-latitude North American Oxisol: estimate of atmospheric CO2 concentration in the Early Eocene "climatic optimum", Geochim. Cosmochim. Ac., 68, 935–947, doi:10.1016/j.gca.2003.09.002, 2004.
Yin, X., Gruber, A., and Arkin, P.: Comparison of the GPCP and CMAP merged gauge–satellite monthly precipitation products for the period 1979–2001, J. Hydrometeorol.,doi:10.1175/JHM-392.1, 2004.
Zachos, J. C., Schouten, S., Bohaty, S., Quattlebaum, T., Sluijs, A., Brinkhuis, H., Gibbs, S. J., and Bralower, T. J.: Extreme warming of mid-latitude coastal ocean during the Paleocene–Eocene Thermal Maximum: inferences from TEX86 and isotope data, Geology, 34, 737–740, doi:10.1130/G22522.1, 2006.
Zachos, J. C., Dickens, G. R., and Zeebe, R. E.: An early Cenozoic perspective on greenhouse warming and carbon-cycle dynamics, Nature, 451, 279–283, 2008.
Zacke, A., Voigt, S., Joachimski, M. M., Gale, A. S., Ward, D. J., and Tutken, T.: Surface-water freshening and high-latitude river discharge in the Eocene North Sea. J. Geol. Soc. London, 166, 969–980, doi:10.1144/0016-76492008-068, 2009.
Zhang, S. and Wang, B.: Global summer monsoon rainy seasons, Int. J. Climatol., 28, 1563–1578, doi:10.1002/joc.1659, 2008.

Figure captions for *Carmichael et al.*

A model-model and model-data comparison for the early Eocene hydrological cycle

Figure 1

Preindustrial precipitation distributions as simulated in the EoMIP models (modern paleogeography) (**a**, **b**, **d**, **f**, **h**, **j** and **l**) show mean annual precipitation (MAP; left colour bar) and (**c**, **e**, **g**, **i**, **k**, and **m**) show anomalies relative to CMAP observations, 1979–2010, GCM output – observations (right colour bar). The inset indicates the principal features of the CMAP precipitation distribution, as discussed in the text.

Figure 2

Global sensitivity of the Eocene hydrological cycle in the EoMIP simulations. Global mean surface air temperature relative to model CO_2 **(a)**, global mean precipitation rate relative to model CO_2 **(b)** and global mean surface air temperature **(c)**; note the logarithmic scale on the horizontal axis in (**a** and **b**). Preindustrial simulations and Eocene simulations are shown as circles and squares respectively. The CCSM3 simulations share a preindustrial simulation, shown in red. Open circle symbols in **(b)** show modern day estimates of global precipitation rate calculated based on CMAP data (red), GPCP data (blue) and Legates and Willmott (1990) climatology (green). Also shown is the sensitivity of the hydrological cycle to global mean surface air temperature in the 17 successful simulations of Sagoo et al. (2013) using FAMOUS (**d**; diamonds), with HadCM3L simulations (blue; Lunt et al., 2010) shown for comparison. All best fit lines are based on Eocene simulations only.

Figure 3.

Mean annual precipitation distributions for each member of the EoMIP ensemble in mm/year (early Eocene paleogeography; ~55 Ma). CO2 for each model simulation is shown above each plot. The FAMOUS simulations are both at 2×CO2.

Figure 4.

Latitudinal temperature and precipitation distributions in the HadCM3L and ECHAM5 (left), CCSM3_H and CCSM3_K (centre) and FAMOUS (right) members of the EoMIP ensemble. **(a–c)** show mean surface air temperature, **(d–f)** total precipitation rate, **(g–i)** convective precipitation and **(j–l)** large-scale precipitation. The HadCM3L, ECHAM5 and CCSM3 atmospheric CO_2 levels are shown in the key. All FAMOUS simulations are at 2 x PI CO2, but differ in value for 10 uncertain parameters (Sect. 2). Simulation names E1–E17 shown in the legend correspond to those given by Sagoo et al. (2013). Black dotted lines show output from preindustrial simulations, with the exception of ECHAM5, shown in orange.

Figure 5

Multimodel mean annual precipitation **(a)** and mean annual precipitation – evaporation rate **(b)** for Eocene (red) and preindustrial (blue) boundary conditions. For the Eocene multimodel mean, simulations have a global mean precipitation rate of 3.40±0.02mmday−1 (Table S1) which are: HadCM3L (×4), HadCM3L_T (×4), ECHAM (×2), CCSM3_H (×4) and a linearly interpolated distribution between the ×4 and ×8 CO2 CCSM3_W simulations. Error bars represent the range in values across simulations.

Figure 6. Anomaly plots for Mean Annual Precipitation mm year−1 between high and low CO2 Eocene model simulations for **(a)** HadCM3L ×6 CO2 – ×2 CO2 and **(b)** CCSM3_W ×16 CO2 – ×4 CO2.

Figure 7. Percentage of mean annual precipitation falling in the extended summer season (MJJAS for Northern Hemisphere, NDJFM for Southern Hemisphere; early Eocene paleogeography); regions with > 55% summer precipitation are outlined in blue. Results from preindustrial simulations are shown in the Supplement. CO2 for each model simulation is shown above each plot. The FAMOUS simulations are both at 2×CO2.

Figure 8. Mean annual *P −E* distributions for each member of the EoMIP ensemble in mm year−1 (early Eocene paleogeography). CO2 for each model simulation is shown above each plot. The FAMOUS simulations are both at 2×CO2.

Figure 9. Latitudinal *E - P* distributions (top) and implied northwards latent heat flux (bottom) in the EoMIP simulations. The black lines indicate preindustrial simulations with dotted and unbroken lines in (**d** and **h**) corresponding to the GISS-ER and ECHAM5 simulations respectively. Heat flux expressed in petawatts (1PW= 1015 W). Observational E – P in (a) is based on ECMWF ERA reanalysis data (Dee et al., 2004).

Figure 10. Proxy-model comparisons for mean annual precipitation (MAP) for the EoMIP ensemble **(a)** Axel Heiberg island, data from Greenwood et al. (2010); **(b)** North West Territories, data from Greenwood et al. (2010); **(c)** South East Australia and Tasmania, data from Greenwood et al. (2005) and Contreras et al. 2014); **(d)** central Europe, data from Mosbrugger et al. (2005) and Grein et al. (2011); **(e)** ODP Site 913, data from Eldrett et al. (2009); **(f)** Wilkes Land, data from Pross et al. (2012); **(g)** Western US interior, data from Wilf et al. (1998) and Wilf (2000); **(h)** Waipara, New Zealand, data from Pancost et al. (2013); **(i)** Mahenge, Tanzania, data from Jacobs and Herendeen (2004) and Kaiser et al. (2006); **(j)** Argentina, data from Wilf et al. (2005) **(k)** Chickaloon Fm, Alaska, data from Sunderlin et al. (2011, 2014); **(l)** Antarctic Peninsula, data from Hunt and Poole (2003) and Poole et al. (2005); **(m)** Cerrejon Formation, data from Wing et al. (2009). Error bars show the mean with range based on nine model grid cells closest to given paleocoordinates. Full details are given in the Supplement, Table S3.

Figure 11. Surface air temperature and mean annual precipitation proxy-model anomalies for low and high CO2 climates shown by closed and open circles respectively. Simulations are at ×2 and ×6 CO2 for HadCM3L **(a)**, E17 for FAMOUS **(b)**, ×2 and ×16 CO2 for CCSM3_H **(c)**, and ×5 and ×9 CO2 for CCSM3_K **(d)**. The data points represent averaged signals for the sites shown in Fig. 10. Estimates of maximum (minimum) error are calculated as anomalies between the highest (lowest) data estimate and the lowest (highest) value within the local model grid.

Figure 12 Summary of regions which show a significant model spread, based on the Eocene multimodel mean described in Figure 5. Paleobotanical estimates of quantitative precipitation rate included in the data compilation are shown by green markers. Regions where the standard deviation is greater than 1 mm/day (i.e. 360 mm/year) are marked by a red outline and regions where the coefficient of variation (standard deviation/multimodel mean) is greater than 40% are outlined blue.

Figure S1 Percentage error between preindustrial model simulated Mean Annual Precipitation and CMAP observational data, calculated as (model-observations)/observations x 100%

Figure S2 Coefficient of variation for preindustrial model simulations, calculated as standard deviation of multi-model mean (n=5) divided by multi-model mean. This is robust against larger standard deviations in regions of higher precipitation.

Figure S3 Changes in mean annual evapotranspiration 4 x CO_2 – 2 CO_2 simulations in HadCM3L in (a) the fixed shrubland simulations of Lunt et al. (2010) and (b) the TRIFFID dynamic vegetation simulations of Loptson et al. (2014). The differences in mean specific humidity relative to air temperature over tropical continents is shown in (c).

Figure S4 Surface pressure and winds over the South Pacific in Eocene simulations (a) HadCM3L, 2 x CO_2 and (b) CCSM3W, 4 x CO_2. The length of vectors is proportional to wind strength. The blue line shows the outline of the region where mean precipitation is greater than 5 mm/day.

Figure S4 Proxy estimates of Mean Annual Precipitation (circles) shown relative to simulated distribution in HadCM3L, 6 x CO_2 (a) and against latitudinally-averaged daily precipitation rate for the four Eocene HadCM3L simulations at x1, x2, x4 and x6 CO_2 (b).

Figure S5 Differences in topography (a – c) and precipitation rate (d – f) in pairs of simulations; HadCM3L 6 x CO2 – CCSM3H 8 x CO2 (a,d); HadCM3L 4 x CO2 – FAMOUS e10 (b,e) and CCSM3H 4 x CO2 and CCSM3W 8xCO2. Simulations are chosen which have similar global precipitation rates (Figure 2).

Figure S6 Vertical velocity of atmosphere averaged over 150°E to 150°W for HadCM3L simulations (left) and CCSM3(W) simulations (right). The bottom figures shows anomalies for the high CO_2 – low CO_2 simulations.

Figure S7 Percentage of mean annual precipitation falling in the extended summer season (MJJAS for northern hemisphere, NDJFM for southern hemisphere) for preindustrial simulations; regions with >55% summer precipitation are outlined in blue.

Figure S8 Variations in the peak extratropical (>25°N/S) latent heat flux in petawatts (1 PW = 10^{15} W) between the EoMIP model simulations relative to global mean surface air temperature and the average difference in surface air temperature between the poles and equator. With the exception of the FAMOUS simulations of Sagoo et al. (2013), we join simulations performed with the same GCM for clarity.

Figure S9 Proxy estimates of mean annual precipitation shown relative to latitudinal precipitation distribution for each of the EoMIP simulations. Model CO_2 or simulation name in the case of FAMOUS are shown above each panel. Preindustrial precipitation is shown as a black dotted line. Geologic data are represented by a lower, central and upper estimate based on combined data for the following sites: Wilkes Land, Antarctic Peninsula, southern Australia, New Zealand, Chile, Tanzania, Colombia, eastern China, continental US, central Europe, North West Territories, Alaska, Site 913 and Axel Heiberg Island. Model estimates from gridboxes corresponding to the paleo-locations are shown as coloured circles.

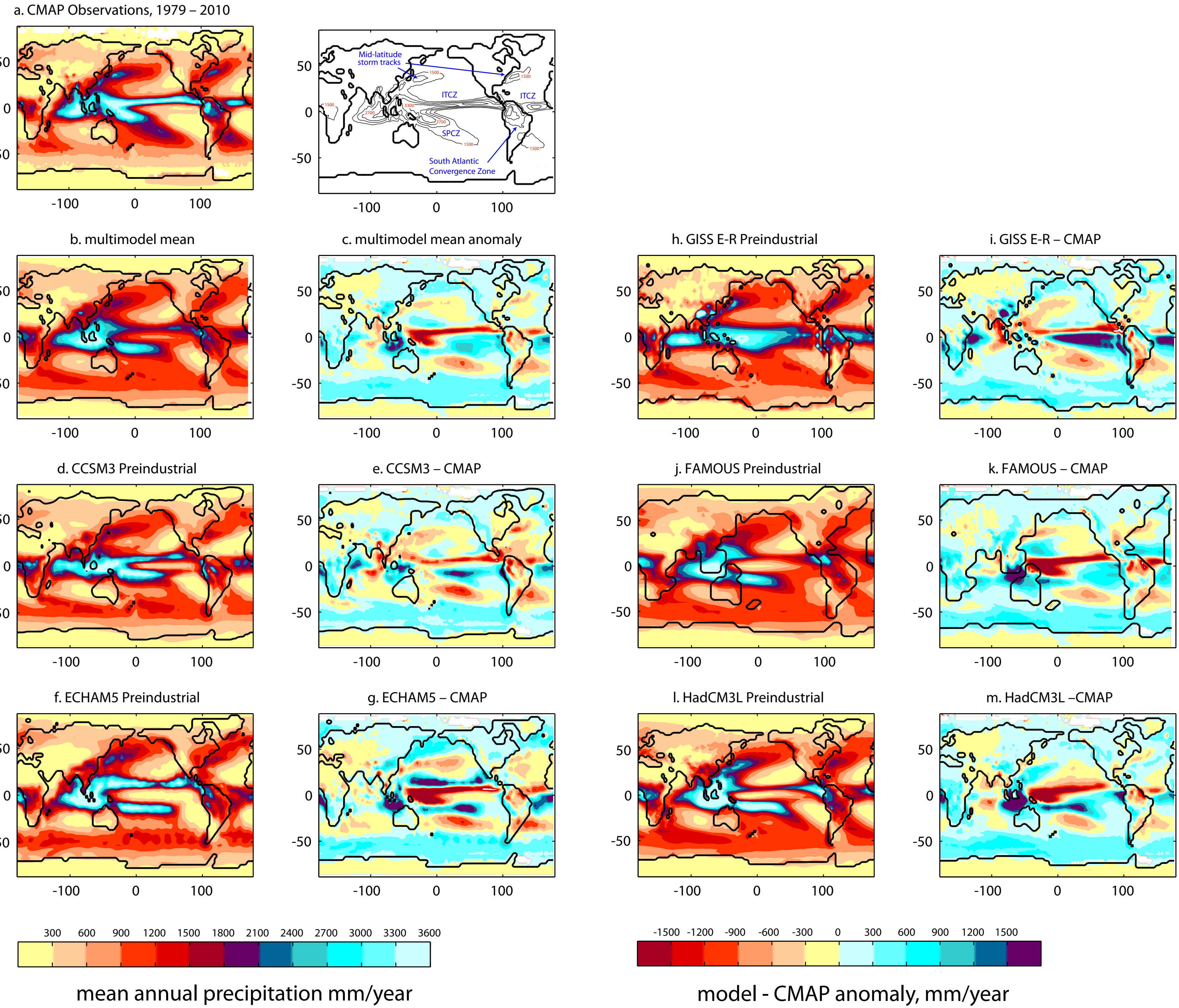

a. CMAP Observations, 1979 – 2010
Mid-latitude storm tracks
ITCZ
ITCZ
SPCZ
South Atlantic Convergence Zone
b. multimodel mean
c. multimodel mean anomaly
h. GISS E-R Preindustrial
i. GISS E-R – CMAP
d. CCSM3 Preindustrial
e. CCSM3 – CMAP
j. FAMOUS Preindustrial
k. FAMOUS – CMAP
f. ECHAM5 Preindustrial
g. ECHAM5 – CMAP
l. HadCM3L Preindustrial
m. HadCM3L –CMAP
300 600 900 1200 1500 1800 2100 2400 2700 3000 3300 3600
mean annual precipitation mm/year
-1500 -1200 -900 -600 -300 0 300 600 900 1200 1500
model - CMAP anomaly, mm/year

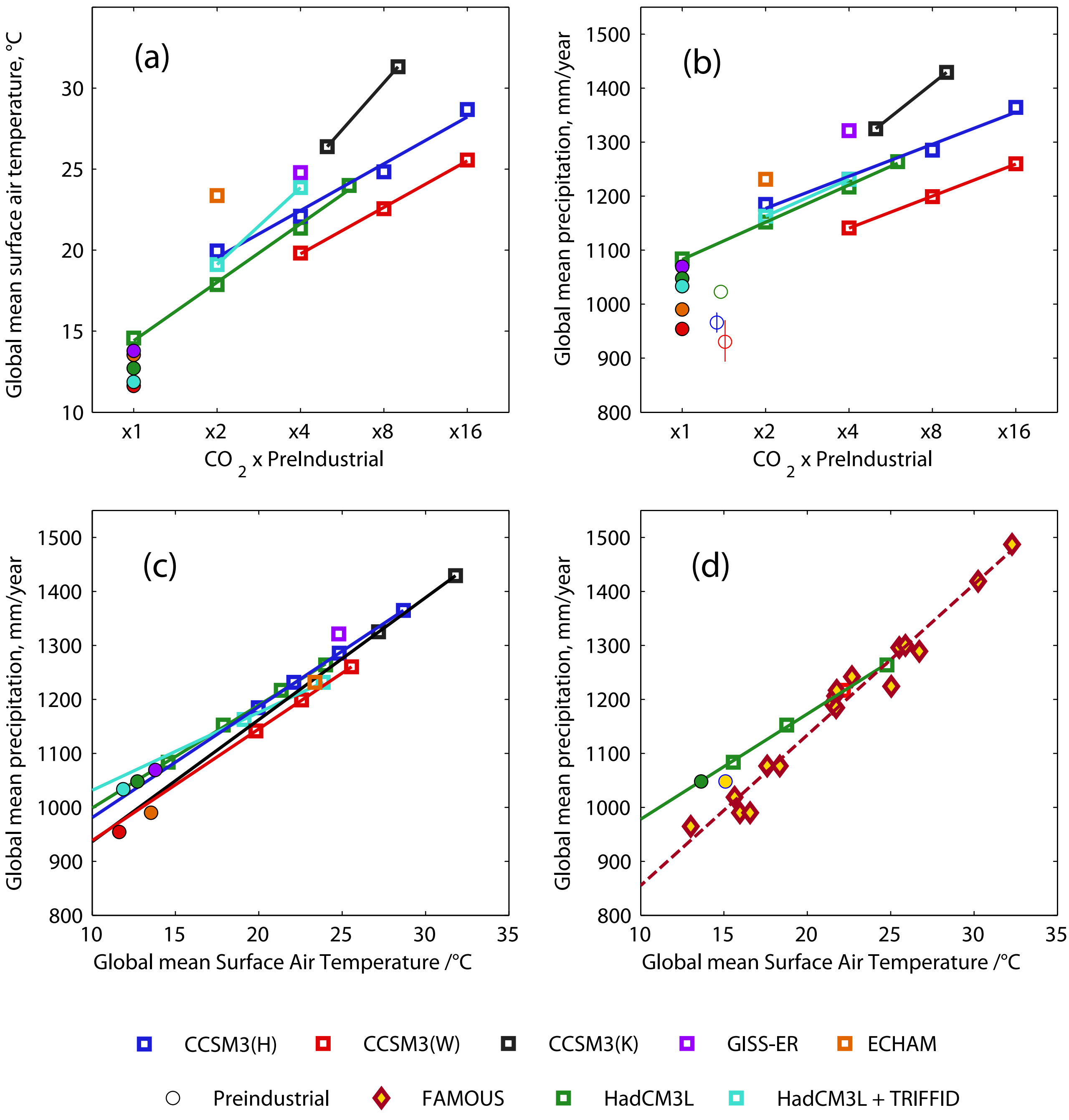
(a)
(b)
(c)
(d)
Global mean surface air temperature, °C
Global mean precipitation, mm/year
CO 2 x PreIndustrial
x1
x2
x4
x8
x16
Global mean Surface Air Temperature /°C
CCSM3(H)
CCSM3(W)
CCSM3(K)
GISS-ER
ECHAM
Preindustrial
FAMOUS
HadCM3L
HadCM3L + TRIFFID

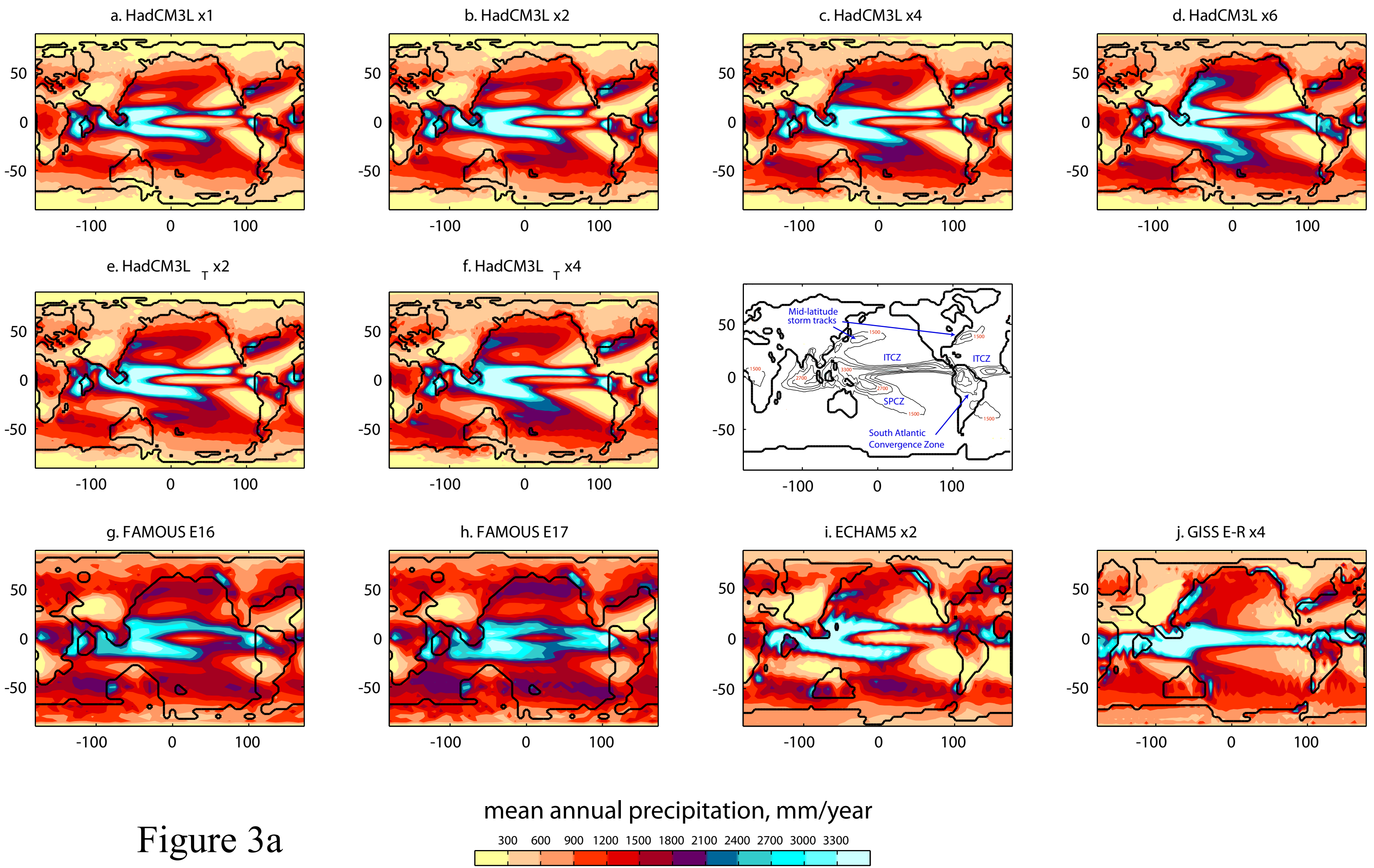
a. HadCM3L x1
b. HadCM3L x2
c. HadCM3L x4
d. HadCM3L x6
e. HadCM3L T x2
f. HadCM3L T x4
Mid-latitude storm tracks
ITCZ
ITCZ
SPCZ
South Atlantic Convergence Zone
g. FAMOUS E16
h. FAMOUS E17
i. ECHAM5 x2
j. GISS E-R x4
mean annual precipitation, mm/year
300 600 900 1200 1500 1800 2100 2400 2700 3000 3300

Figure 3a

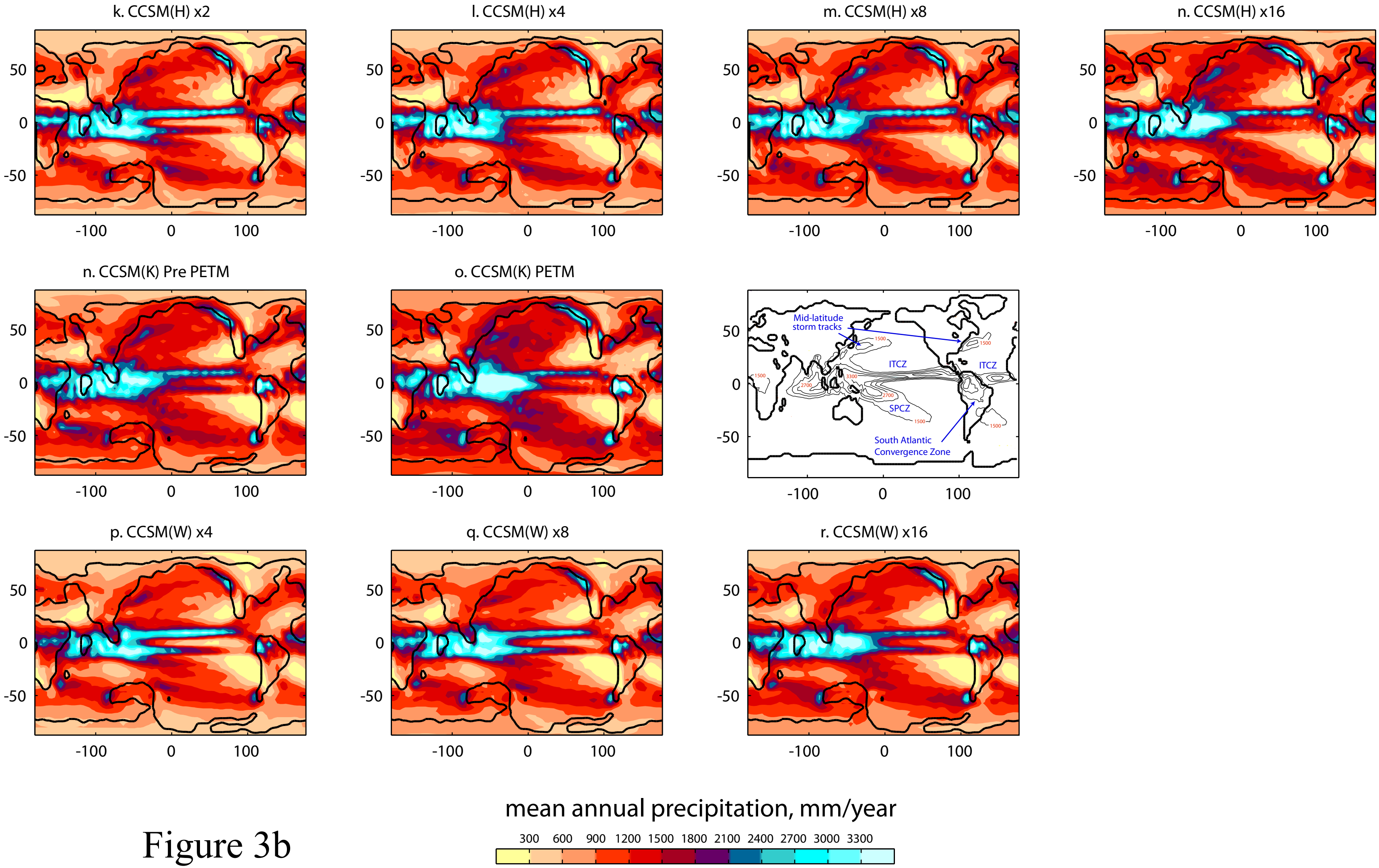
k. CCSM(H) x2
l. CCSM(H) x4
m. CCSM(H) x8
n. CCSM(H) x16
n. CCSM(K) Pre PETM
o. CCSM(K) PETM
p. CCSM(W) x4
q. CCSM(W) x8
r. CCSM(W) x16
50
0
-50
-100
0
100
Mid-latitude
storm tracks
ITCZ
ITCZ
SPCZ
South Atlantic
Convergence Zone
1500
2700
3300
mean annual precipitation, mm/year
300 600 900 1200 1500 1800 2100 2400 2700 3000 3300

Figure 3b

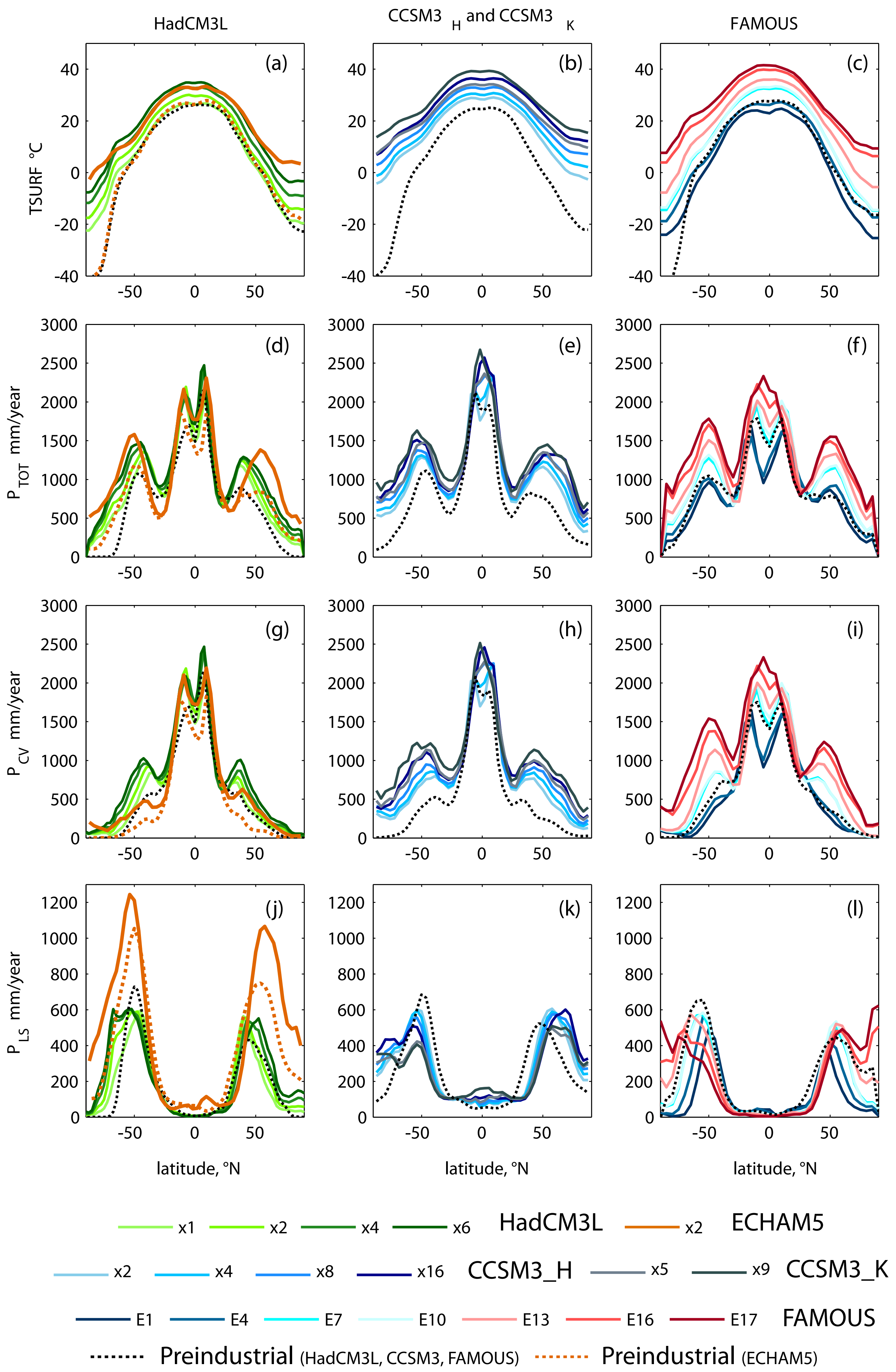
HadCM3L
CCSM3_H and CCSM3_K
FAMOUS
TSURF °C
P_TOT mm/year
P_CV mm/year
P_LS mm/year
latitude, °N
(a) (b) (c) (d) (e) (f) (g) (h) (i) (j) (k) (l)
x1 x2 x4 x6 HadCM3L x2 ECHAM5
x2 x4 x8 x16 CCSM3_H x5 x9 CCSM3_K
E1 E4 E7 E10 E13 E16 E17 FAMOUS
Preindustrial (HadCM3L, CCSM3, FAMOUS) Preindustrial (ECHAM5)

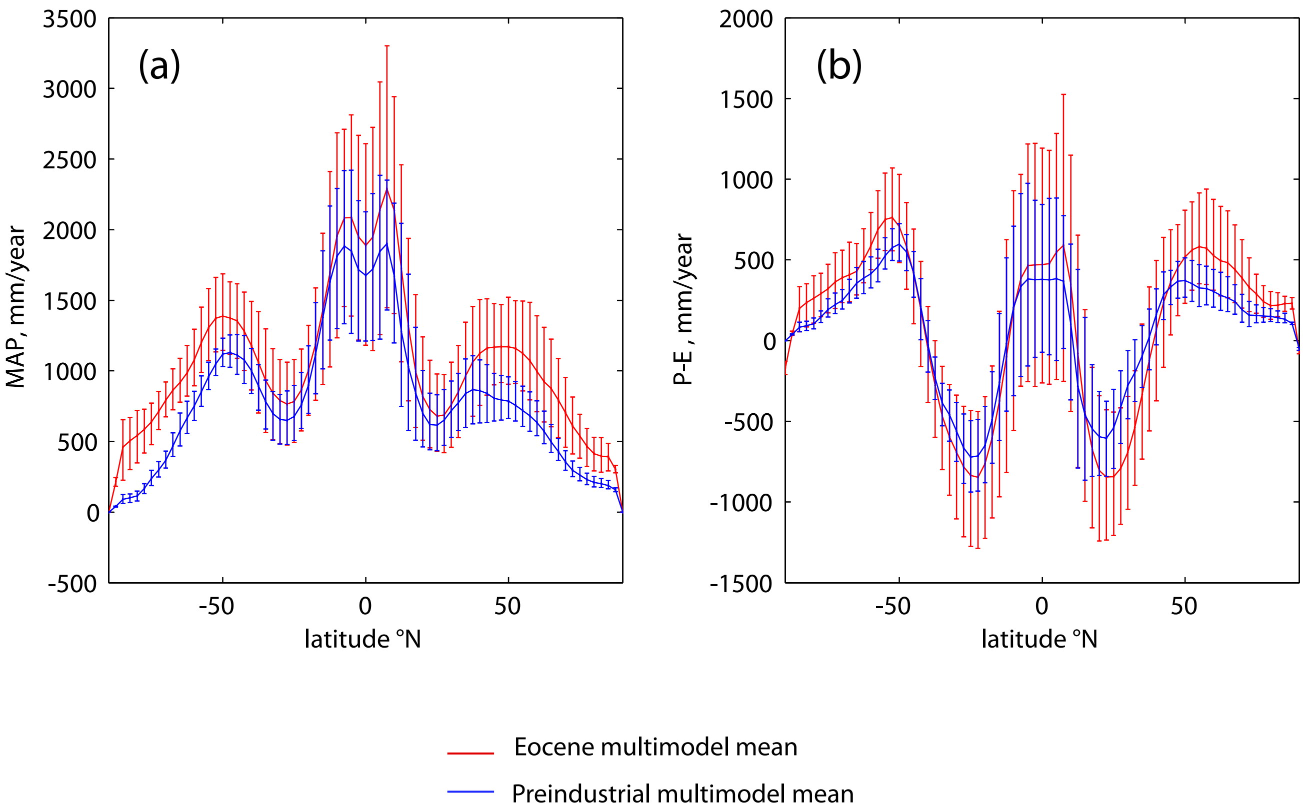
(a)
MAP, mm/year
3500
3000
2500
2000
1500
1000
500
0
-500
-50
0
50
latitude °N
(b)
P-E , mm/year
2000
1500
1000
500
0
-500
-1000
-1500
-50
0
50
latitude °N
Eocene multimodel mean
Preindustrial multimodel mean

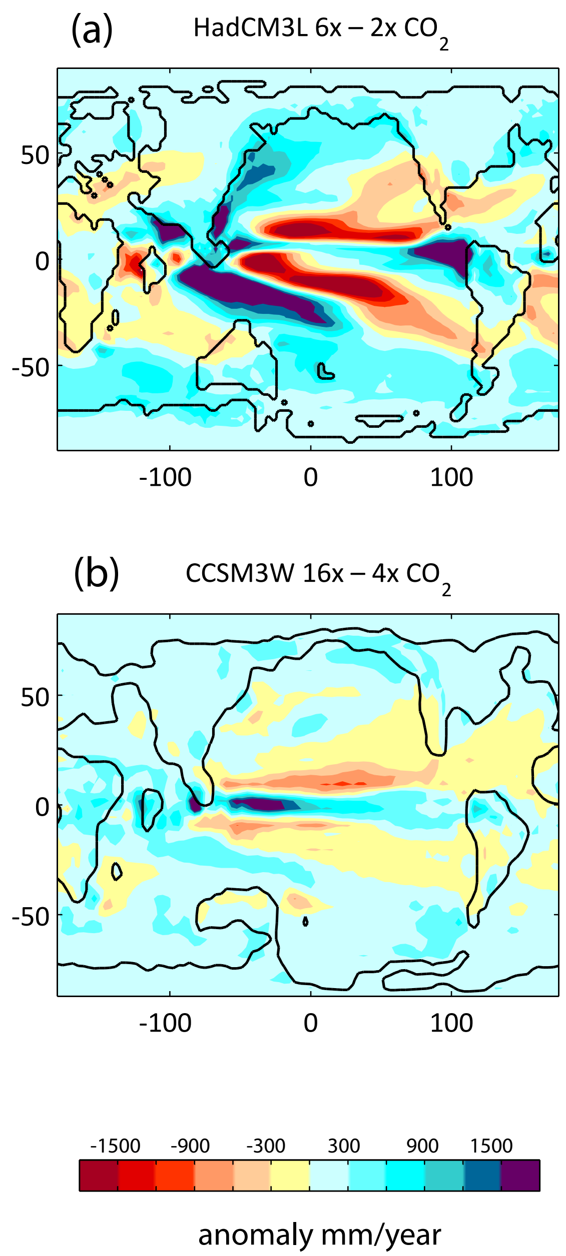
(a)
HadCM3L 6x – 2x CO_2
50
0
-50
-100
0
100
(b)
CCSM3W 16x – 4x CO_2
50
0
-50
-100
0
100
-1500
-900
-300
300
900
1500
anomaly mm/year

Figure 6

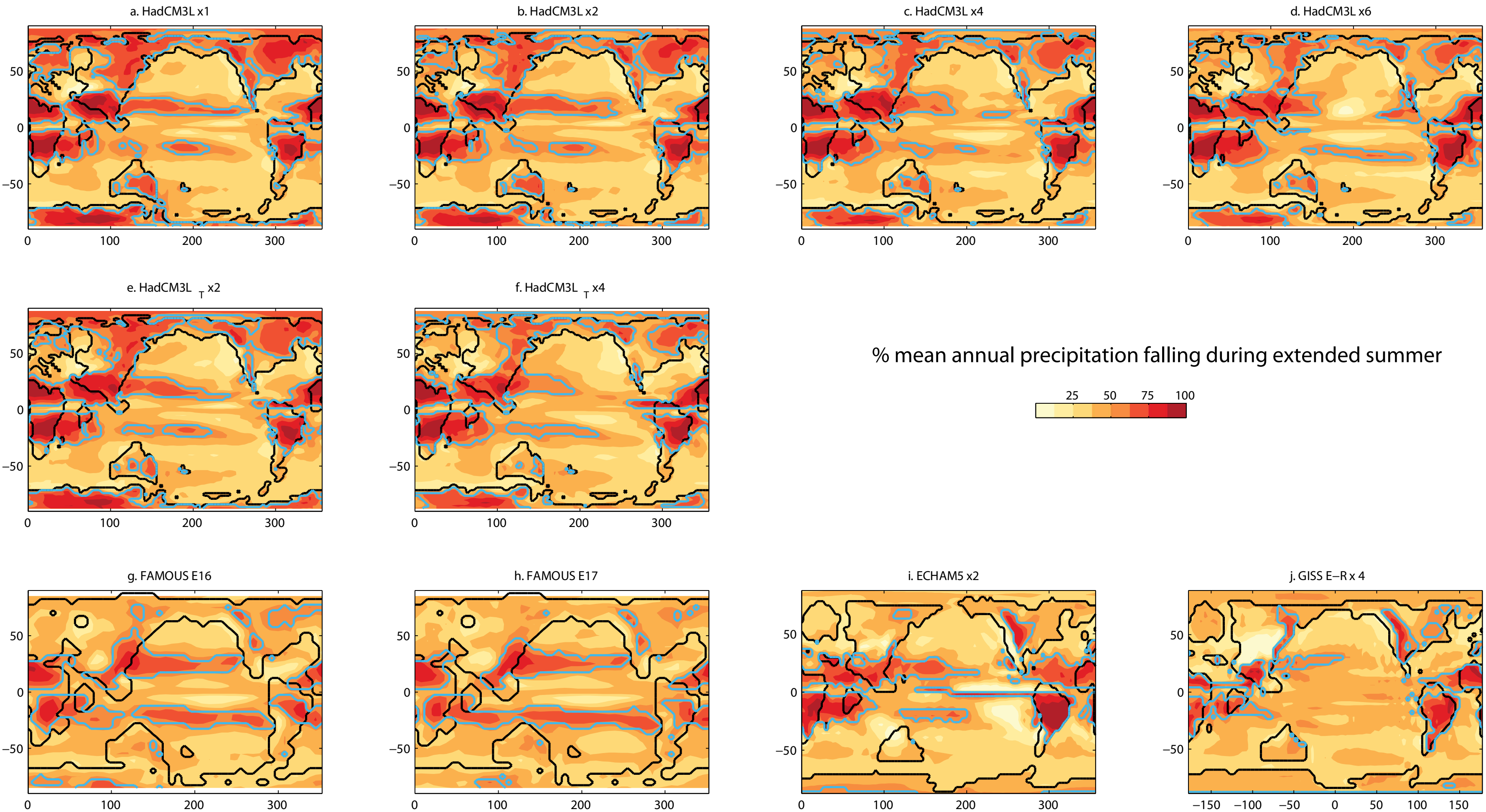
a. HadCM3L x1
b. HadCM3L x2
c. HadCM3L x4
d. HadCM3L x6
e. HadCM3L T x2
f. HadCM3L T x4
% mean annual precipitation falling during extended summer
25
50
75
100
g. FAMOUS E16
h. FAMOUS E17
i. ECHAM5 x2
j. GISS E−R x 4

Figure 7a

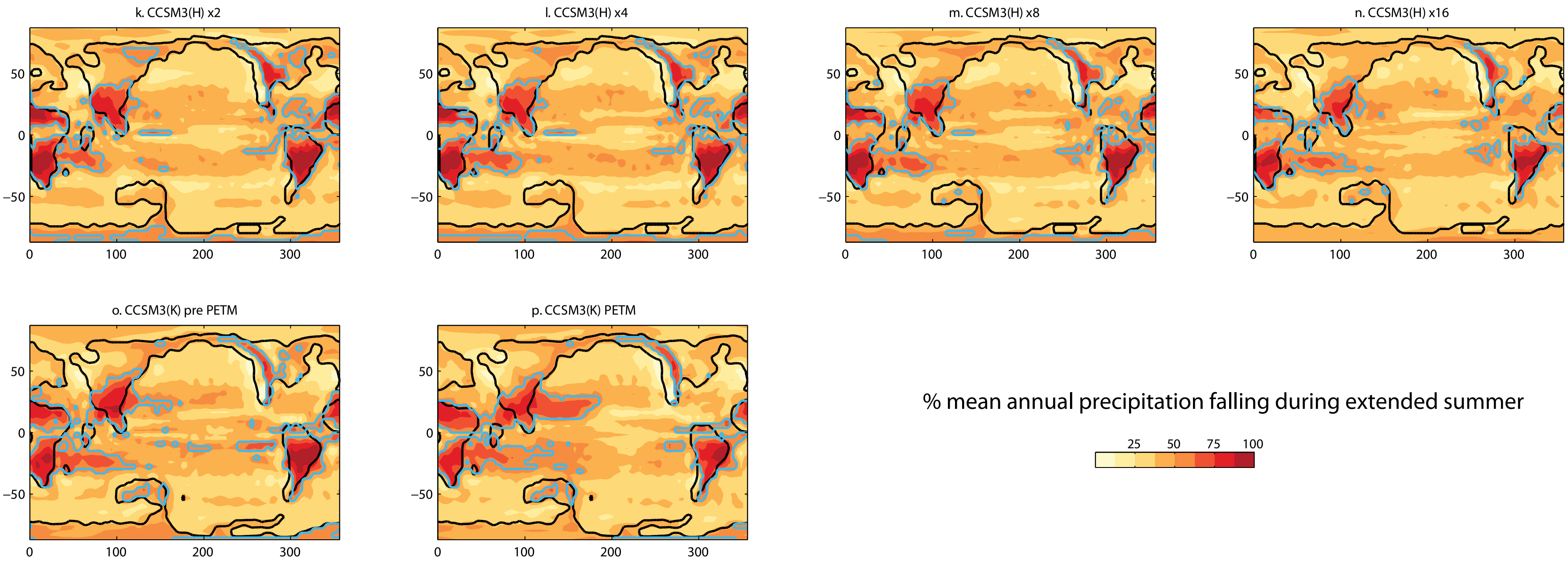
k. CCSM3(H) x2
l. CCSM3(H) x4
m. CCSM3(H) x8
n. CCSM3(H) x16
o. CCSM3(K) pre PETM
p. CCSM3(K) PETM
% mean annual precipitation falling during extended summer
25
50
75
100

Figure 7b

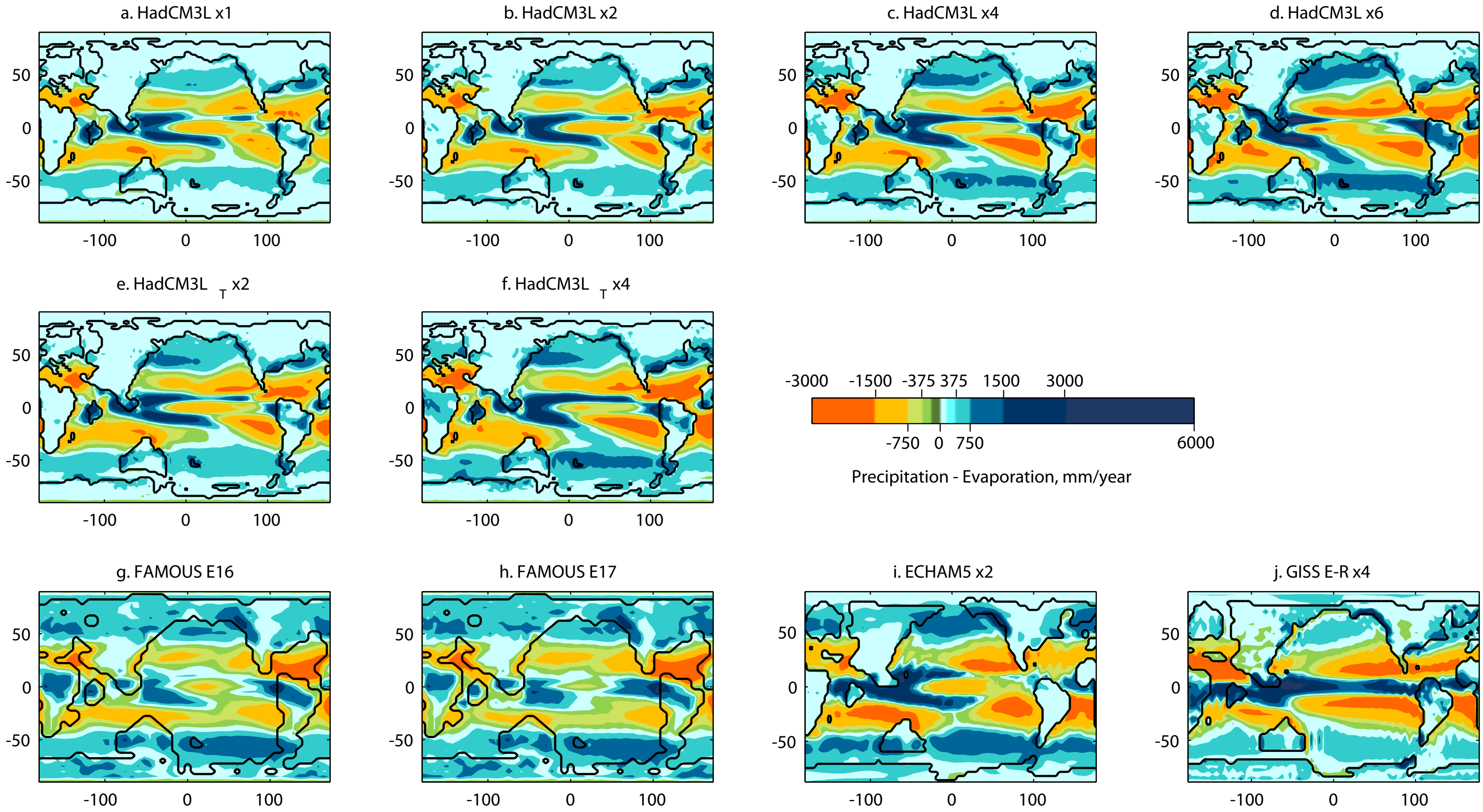

a. HadCM3L x1
b. HadCM3L x2
c. HadCM3L x4
d. HadCM3L x6
e. HadCM3L T x2
f. HadCM3L T x4
g. FAMOUS E16
h. FAMOUS E17
i. ECHAM5 x2
j. GISS E-R x4
50
0
-50
-100
0
100
-3000 -1500 -375 375 1500 3000
-750 0 750 6000
Precipitation - Evaporation, mm/year

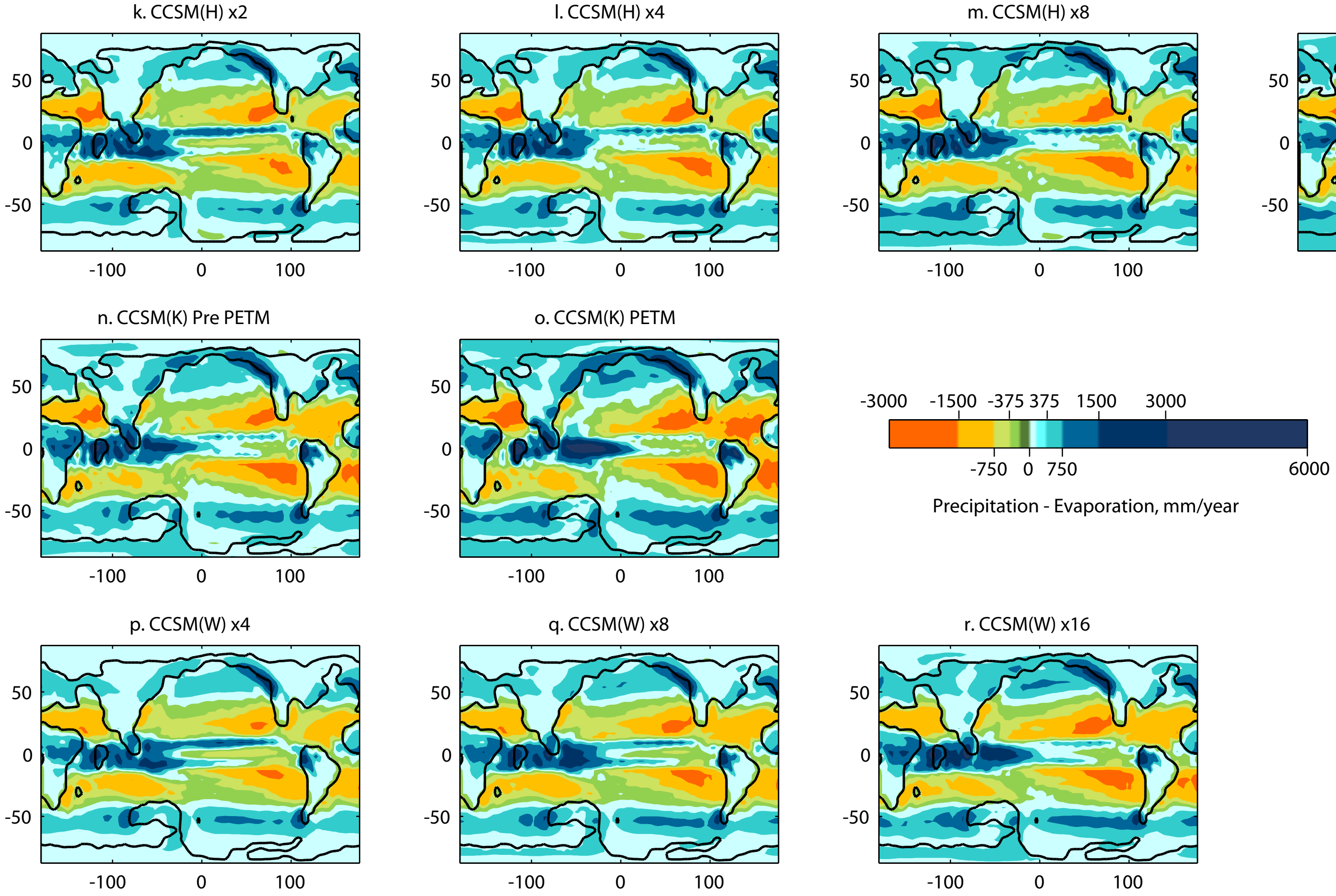
k. CCSM(H) x2
l. CCSM(H) x4
m. CCSM(H) x8
n. CCSM(H) x16
n. CCSM(K) Pre PETM
o. CCSM(K) PETM
p. CCSM(W) x4
q. CCSM(W) x8
r. CCSM(W) x16
50
0
-50
-100
0
100
-3000
-1500
-375
375
1500
3000
-750
0
750
6000
Precipitation - Evaporation, mm/year

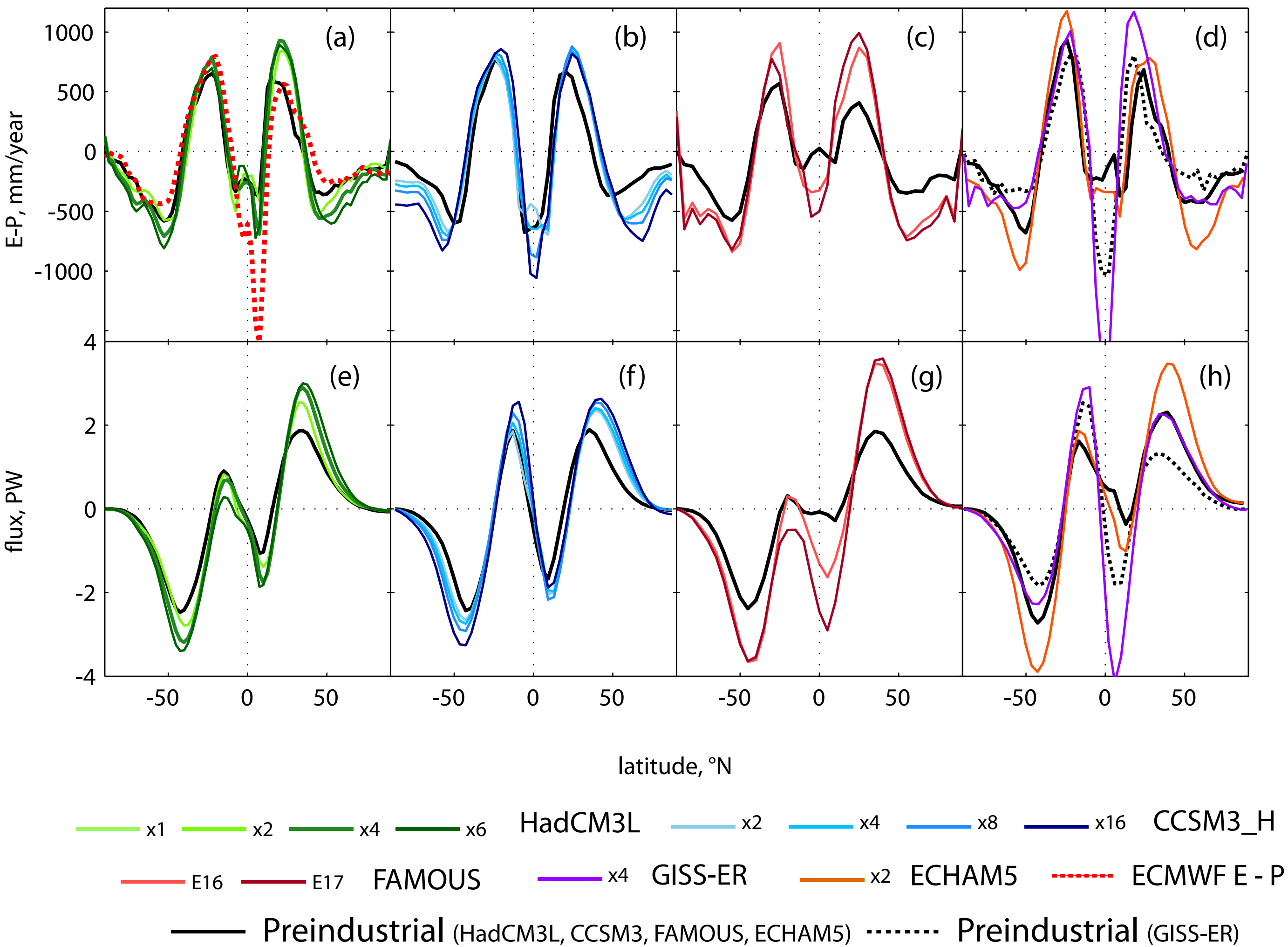

E-P, mm/year
flux, PW
latitude, °N
(a)
(b)
(c)
(d)
(e)
(f)
(g)
(h)
x1 x2 x4 x6 HadCM3L
x2 x4 x8 x16 CCSM3_H
E16 E17 FAMOUS
x4 GISS-ER
x2 ECHAM5
ECMWF E - P
Preindustrial (HadCM3L, CCSM3, FAMOUS, ECHAM5)
Preindustrial (GISS-ER)

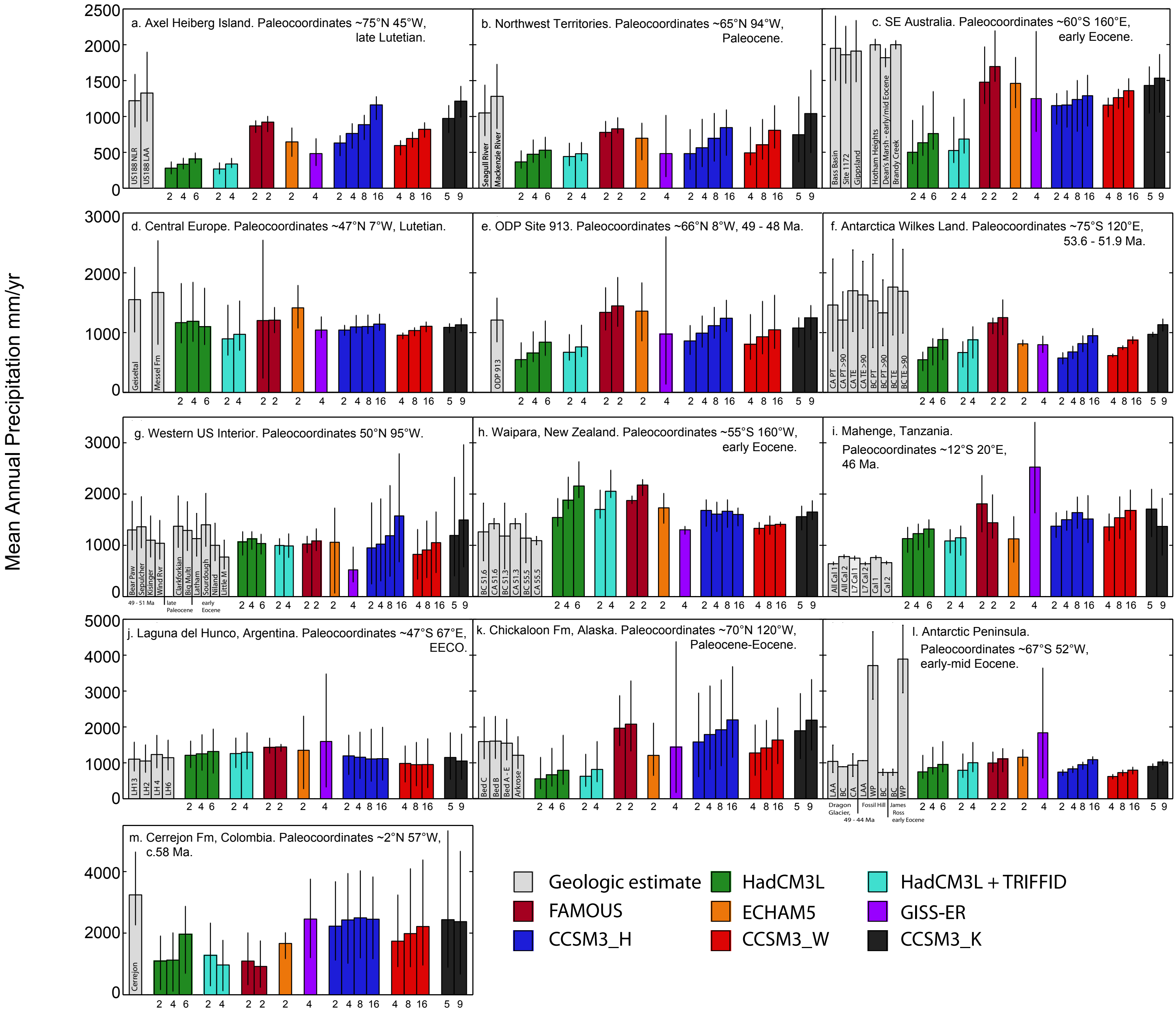
Mean Annual Precipitation mm/yr
a. Axel Heiberg Island. Paleocoordinates ~75°N 45°W, late Lutetian.
b. Northwest Territories. Paleocoordinates ~65°N 94°W, Paleocene.
c. SE Australia. Paleocoordinates ~60°S 160°E, early Eocene.
d. Central Europe. Paleocoordinates ~47°N 7°W, Lutetian.
e. ODP Site 913. Paleocoordinates ~66°N 8°W, 49 - 48 Ma.
f. Antarctica Wilkes Land. Paleocoordinates ~75°S 120°E, 53.6 - 51.9 Ma.
g. Western US Interior. Paleocoordinates 50°N 95°W.
h. Waipara, New Zealand. Paleocoordinates ~55°S 160°W, early Eocene.
i. Mahenge, Tanzania. Paleocoordinates ~12°S 20°E, 46 Ma.
j. Laguna del Hunco, Argentina. Paleocoordinates ~47°S 67°E, EECO.
k. Chickaloon Fm, Alaska. Paleocoordinates ~70°N 120°W, Paleocene-Eocene.
l. Antarctic Peninsula. Paleocoordinates ~67°S 52°W, early-mid Eocene.
m. Cerrejon Fm, Colombia. Paleocoordinates ~2°N 57°W, c.58 Ma.
Geologic estimate
HadCM3L
HadCM3L + TRIFFID
FAMOUS
ECHAM5
GISS-ER
CCSM3_H
CCSM3_W
CCSM3_K

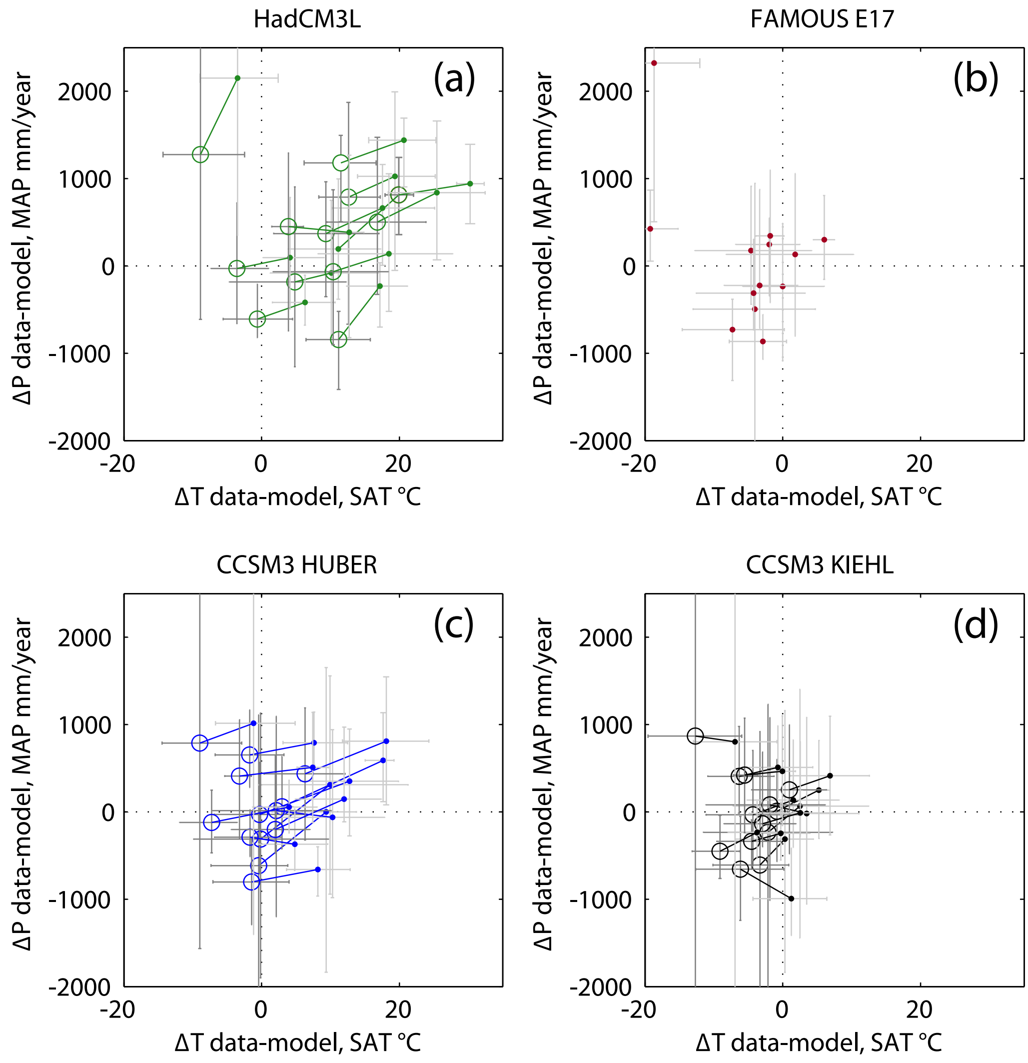

HadCM3L
(a)
FAMOUS E17
(b)
CCSM3 HUBER
(c)
CCSM3 KIEHL
(d)
ΔP data-model, MAP mm/year
ΔT data-model, SAT °C
2000
1000
0
-1000
-2000
-20
0
20

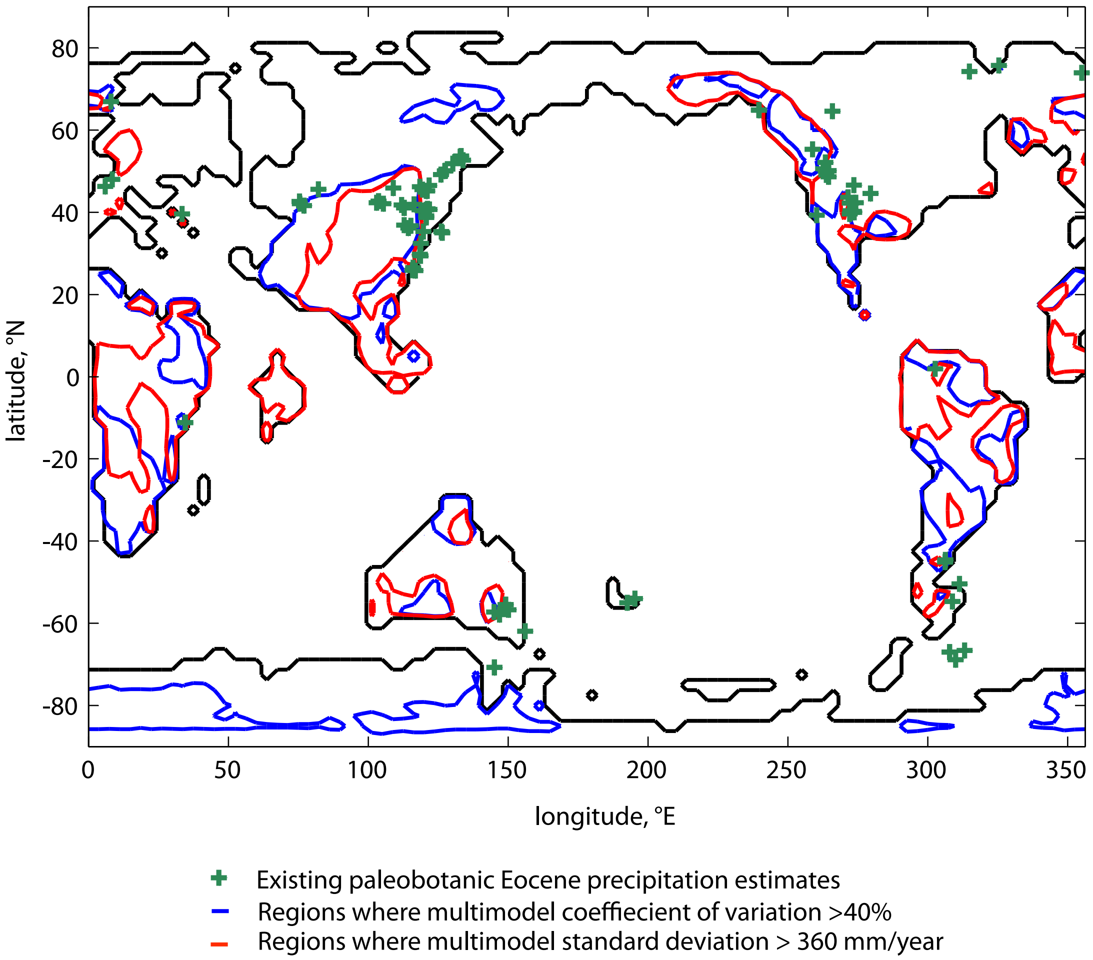

80
60
40
20
0
-20
-40
-60
-80
latitude, °N
0
50
100
150
200
250
300
350
longitude, °E
Existing paleobotanic Eocene precipitation estimates
Regions where multimodel coeffiecient of variation >40%
Regions where multimodel standard deviation > 360 mm/year

Model	Eocene simulation reference	Model reference	Atmosphere resolution	Ocean resolution	Paleogeography	Sim. length (years)	CO_2 levels	Orbital configuration
HadCM3L HadCM3L (T)	Lunt et al. (2010) Loptson et al. (2014)	Cox et al. (2001)	96 x 73 x 19	96 x 73 x 20	Proprietary	> 3400	x 1,2,4,6 x 2,4	Preindustrial orbit.
ECHAM5	Heinemann et al. (2009)	Roeckner et al. (2003)	96 x 48 x 19	142 x 82 x 40	Bice and Marotzke (2001)	2500	x 2	*e* = 0.0300; *o* = 23.25; *p* = 270
CCSM3 (W)	Winguth et al. (2010, 2012)	Collins et al. (2006); Yeager et al. (2006)	96 x 48 x 26	100 x 116 x 25	Sewall et al. (2000) with marginal sea parameterisation	1500	x 4,8,16	*e = 0; o* = 23.5;
CCSM3 (H)	Liu et al. (2009); Huber and Caballero (2011)	Collins et al. (2006); Yeager et al. (2006)	96 x 48 x 26	100 x 122 x 25	Sewall et al. (2000)	1500	x2,4,8,16	Preindustrial orbit.
CCSM3 (K)	Kiehl and Shields (2013)	Collins et al. (2006); Yeager et al. (2006)	96 x 48 x 26	100 x 116 x 25	As CCSM(W)	>2000 > 3600 +	x~5 x ~9	As CCSM(W)
GISS E-R	Roberts et al. (2009)	Schmidt et al. (2006)	72 x 45 x 20	72 x 45 x 13	Bice and Marotzke (2001)	2000	x ~4	*e* = 0.0270; *o* = 23.20, *p* = 180
FAMOUS	Sagoo et al. (2013)	Jones et al. (2005), Smith et al. (2008).	48 x 37 x 11	96 x 73 x 20	Proprietary	> 1500	x 2	Preindustrial orbit.

Model	Stratiform precipitation	Convective precipitation	Vegetation	Aerosols
HadCM3	Large-scale precipitation is calculated based on cloud water and ice contents (similar to Smith, 1990)	Bulk mass flux scheme (Gregory and Rowntree, 1990), with improvement by Gregory et al. (1997)	Homogenous shrubland (Lunt) Dynamically evolving vegetation TRIFFID (Loptson)	As control
ECHAM5	Prognostic equations for the water phases, bulk cloud microphysics (Lohmann and Roeckner, 1996)	Bulk mass flux scheme (Tiedtke 1989) with modifications for deep convection according to Nordeng (1994).	Homogenous woody savannah	As control
CCSM_W	Prognostic condensate and precipitation parameterisation (Zhang et al., 2003)	Simplified Arakawa and Schubert (1974) (cumulus ensemble) scheme developed by Zhang and McFarlane (1995)	Shellito and Sloan (2006)	As control
CCSM_H			Sewall et al. (2000)	Reduced aerosol loading.
CCSM_K			Sewall et al. (2000)	Cloud microphysical parameters altered.
GISS E-R	Prognostic stratiform cloud based on moisture convergence (Del Genio et al. 1996)	Bulk mass flux scheme by Del Genio and Yao (1993)	Sewall et al. (2000)	As control
FAMOUS	Precipitation parameterisation schemes are based on those of HadCM3.		Homogenous shrubland.	Uncertain perturbed parameters include those relating to cloud microphysical properties.

Table 1 Summary of model simulations in the ensemble adapted from Table 1 of Lunt et al. (2012). Additions detailing precipitation schemes are from Table 2 of Dai (2006). Some models have irregular grids in the atmosphere and/or ocean, or have spectral atmospheres. The atmospheric and ocean resolution are given in number of gridboxes, X x Y x Z where X is the effective number of gridboxes in the zonal, Y in the meridional, and Z in the vertical. *e* = eccentricity; *o* = obliquity; *p* = longitude of perihelion.

Model simulations	**P-T regression***	**% increase P per °C warming over range****
HadCM3L	$P = 19.51\ T + 782.89$	1.81
HadCM3L(T)	$P = 14.33\ T + 874.01$	1.32
CCSM3_H	$P = 21.38\ T + 738.22$	2.02
CCSM3_K	$P = 22.61\ T + 710.60$	2.15
CCSM3_W	$P = 21.46\ T + 696.28$	2.11
FAMOUS	$P = 27.86\ T + 576.22$	2.80

Table 2 Summary of relationships between global surface air temperature and precipitation rate. *T = SAT °C, P = global precipitation mm/year.
** Precipitation sensitivity is calculated over the range of 15 – 30°C.

Model	PI	x1 CO_2	x2 CO_2	x4/5 CO_2	x6/8/9 CO_2	x16 CO_2
HadCM3L	60.1	66.3	62.6	57.7	52.3	
HadCM3L(T)			62.0	51.6		
ECHAM5	50.1		41.6			
GISS E-R	47.7			37.6		
CCSM(H)	50.1		47.3	44.2	42.4	35.1
CCSM(K)				47.5	34.12	
FAMOUS	48.9		28.1 E16 23.6 E17			

Table 3 % land surface characterised by extended summer precipitation > 55% MAP